Deciphering the Cenozoic Exhumation History of the Eastern Pyrenees Along a Crustal-Scale Normal Fault Using Low-Temperature Thermochronology

Gaétan Milesi, Patrick Monie, Roger Soliva, P. Münch, Pierre Valla, Stéphanie Brichau, Michaël Bonno, Céline Martin, Mathieu Bellanger

Tectonics

RESEARCH ARTICLE
10.1029/2021TC007172

Key Points:

- Tectonic evolution along a major normal fault recorded by low-temperature thermochronology
- Priabonian (35–32 Ma) switch between contractional and extensional regime in the Eastern Pyrenees
- Cenozoic westward propagation of the deformation along the Têt fault

Supporting Information:

Supporting Information may be found in the online version of this article.

Correspondence to:

G. Milesi,
gaetan.milesi@univ-fcomte.fr

Citation:

Milesi, G., Monié, P., Soliva, R., Münch, P., Valla, P. G., Brichau, S., et al. (2022). Deciphering the Cenozoic exhumation history of the Eastern Pyrenees along a crustal-scale normal fault using low-temperature thermochronology. *Tectonics*, *41*, e2021TC007172. https://doi.org/10.1029/2021TC007172

Received 13 DEC 2021
Accepted 19 MAR 2022

Author Contributions:

Conceptualization: G. Milesi, P. Monié, R. Soliva, P. Münch, M. Bellanger
Data curation: G. Milesi, P. Monié, R. Soliva, P. Münch, P. G. Valla
Formal analysis: G. Milesi, P. Monié, R. Soliva, P. Münch, P. G. Valla, S. Brichau, M. Bonno, C. Martin, M. Bellanger
Funding acquisition: G. Milesi, R. Soliva, M. Bellanger
Investigation: G. Milesi, P. Monié, R. Soliva, P. Münch, P. G. Valla, S. Brichau, M. Bonno, C. Martin, M. Bellanger
Methodology: G. Milesi, P. Monié, R. Soliva, P. Münch, M. Bonno, C. Martin
Project Administration: G. Milesi, R. Soliva, M. Bellanger

Deciphering the Cenozoic Exhumation History of the Eastern Pyrenees Along a Crustal-Scale Normal Fault Using Low-Temperature Thermochronology

G. Milesi[1,2], P. Monié[1], R. Soliva[1], P. Münch[1], P. G. Valla[3], S. Brichau[4], M. Bonno[1], C. Martin[1], and M. Bellanger[5]

[1]Géosciences Montpellier, Université de Montpellier, CNRS, Université des Antilles, Montpellier, France, [2]Chrono-Environnement, UMR 6249-CNRS, Université Bourgogne Franche-Comté, Besançon, France, [3]University of Grenoble Alpes, University of Savoie Mont Blanc, CNRS, IRD, IFSTTAR, ISTerre, Grenoble, France, [4]Geosciences Environnement Toulouse (GET), Université de Toulouse, UPS, University Paul Sabatier, CNRS, IRD, CNES, Toulouse, France, [5]TLS Geothermics, Toulouse, France

Abstract The timing of transition between the contractional and extensional regimes along the Pyrenean range remains debated. Compared to its central and western parts, the eastern part of the chain was significantly affected by extensional tectonics mostly related to the opening of the Gulf of Lion. The Têt normal fault is the best example of this tectonic activity, with topographic reliefs above 2,000 m in its footwall. In this study, we synthetized previous thermochronological data and performed new (U-Th)/He and fission track dating in the Eastern Pyrenean massifs. Output apparent exhumation rate and thermal modeling in the hanging wall of the Têt fault highlight a rapid exhumation (0.48 km/Ma) and cooling (~30°C/Ma) phase between 38 and 35 Ma, followed by slower exhumation/cooling afterward. In the footwall, cooling subsequently propagated westward along the fault during Priabonian (35–32 Ma), upper Oligocene and lower Miocene (26–19 Ma), and Serravallian-Tortonian times (12–9 Ma). These data and modeling outcomes suggest that the exhumation of the Têt fault hanging wall related to southward thrusting ended at 35 Ma, and was followed by different extensional stages, with a propagation of the deformation toward the West during the upper Miocene. We propose that the onset of extension in the Eastern Pyrenees occurred during the late Priabonian period, contemporaneously with the large-scale rifting episode recorded in Western Europe. After this event, the Têt fault activity and the westward propagation of the deformation appear mainly controlled by the opening of the Gulf of Lion.

Plain Language Summary The Pyrenees result from the North-South convergence of the Eurasian and Iberian plates. The eastern part of the range experienced strong extensional tectonics mostly related to the opening of the Gulf of Lion, which timing and influence on the modern topographic relief remain unclear. To better characterize the transition timing between contractional and extensional regimes and the tectonic evolution in the Eastern Pyrenees, we used low-temperature thermochronology and thermal modeling to reconstruct the exhumation/cooling histories of the different massifs along the Têt fault. Our data and modeling outcomes show a switch between contractional and extensional tectonics during the Priabonian (ca. 35 Ma), followed by different extensional stages recorded in the Têt fault footwall, coeval with a global westward propagation of the deformation along the fault until ca. 9 Ma.

1. Introduction

In orogenic belts, crustal-scale faults are key deformation markers that accommodate various regimes of plate tectonics during rock burial, exhumation or strike slip activity (Jones & Wesnousky, 1992; Malusà et al., 2009; Norris & Cooper, 2001; Ratschbacher et al., 2003; Viola et al., 2004). When syn-to post-orogenic sedimentary record or chronological constraints are lacking for bracketing fault activity within orogens, low-temperature (low-T) thermochronology is a powerful tool to quantify the timing and magnitude of exhumation along major faults, since it provides time constraints on the thermal evolution of rocks during their exhumation toward the Earth's surface (Colgan et al., 2006; Ehlers & Farley, 2003; Farley, 2002; Glotzbach et al., 2011; Malusà et al., 2005; Reiners & Brandon, 2006; Stockli, 2005). This situation is common within orogens for which the transition between syn- and post-orogenic periods, or the transition from contraction to extension, remains difficult to date and is often highly debated (Carmignani & Kligfield, 1990; Jolivet, Menant, et al., 2021; Jolivet et al., 2020;

Resources: G. Milesi, P. Monié, R. Soliva, P. Münch, P. G. Valla
Software: G. Milesi, P. Münch, P. G. Valla
Supervision: G. Milesi, P. Monié, R. Soliva
Validation: G. Milesi, P. Monié, R. Soliva, P. Münch, P. G. Valla, S. Brichau, M. Bonno, C. Martin
Visualization: G. Milesi, P. Monié, R. Soliva
Writing – original draft: G. Milesi
Writing – review & editing: G. Milesi, P. Monié, R. Soliva, P. Münch, P. G. Valla, S. Brichau, M. Bonno, C. Martin, M. Bellanger

Price & Henry, 1984; Séranne et al., 2021). Low-T thermochronology has been widely used in large-scale extensional domains to date the activity of normal faults, as for example, in the Basin and Range Province (Armstrong et al., 2003; Colgan et al., 2008; Foster & John, 1999; Surpless et al., 2002) or the Aegean domain (Brichau et al., 2006; Coutand et al., 2014). However, few studies have investigated the onset of post-orogenic extension using low-T thermochronology (i.e., Cederbom et al., 2000; Danišík et al., 2012; Fillon et al., 2021; Martín-González et al., 2012) and even less on the lateral migration of the tectonic activity along normal faults in orogenic context (Curry et al., 2016; Deeken et al., 2006; Krugh, 2008).

In the Pyrenees, previous thermochronological studies have focused mainly on the central part of the chain, which is composed of a stack of crustal nappes formed during the main Eocene—early Oligocene orogenic build up (Bosch et al., 2016; Jolivet et al., 2007; Labaume et al., 2016; Mouthereau et al., 2014; Vacherat et al., 2016, Waldner et al., 2021). In the eastern part of the Pyrenees, less studies have been carried out (Gunnell et al., 2009; Maurel et al., 2002, 2008), which do not provide a detailed view of fault activity through time. This orogen segment shows a similar nappe structure as further West (Calvet et al., 2021; Laumonier et al., 2015, 2017) but has experienced significant post-orogenic crustal thinning to 25 km of total thickness, as indicated by recent geophysical data (Chevrot et al., 2018; Diaz et al., 2018; Lacan & Ortuño, 2012; Nercessian et al., 2001). This thinning is assigned to the presence of numerous and widely distributed normal faults onshore and offshore (Calvet et al., 2021; Jolivet, Menant, et al., 2021; Jolivet et al., 2020; Romagny et al., 2020; Séranne et al., 2021; Taillefer et al., 2021). The geodynamic origin for the onset of the extension has been linked to either the initiation of the West European Rifting which formed a large intraplate feature (Angrand & Mouthereau, 2021; Mouthereau et al., 2021) or the early onset of back-arc extension leading to the formation of the Gulf of Lion (Séranne, 1999; Séranne et al., 2021) The Têt fault is the most prominent normal fault of the Eastern Pyrenees, which localizes high-relief massifs in its footwall such as the Canigou and Carança (Figure 1). The development of these high topographic reliefs has been attributed to normal faulting during the Oligo-Miocene period (Maurel et al., 2008). However, the pre-extensional history of this area, the onset of extension and its polyphase activity along strike during the Cenozoic are still poorly understood (e.g., Angrand & Mouthereau, 2021; Huyghe et al., 2020; Jolivet, Baudin, et al., 2021; Jolivet, Menant, et al., 2021; Jolivet et al., 2020; Taillefer et al., 2021).

In this study, we present a new low-T thermochronology data set from bedrock samples collected on both sides of the Têt fault, including (U-Th)/He on apatite (AHe) and zircon (ZHe), and apatite fission track (AFT). Low-T thermochronological data from previous studies (Gunnell et al., 2009; Maurel et al., 2002, 2008; Milesi, Monié, Münch, et al., 2020; Milesi, Monié, Soliva, et al., 2020; Milesi et al., 2019) have been also synthesized with the new data set, and all data are used for thermal modeling to assess the exhumation history of the footwall and hanging wall massifs along the southwestern segment of the Têt fault. Based on these results, we discuss the onset, timing, and spatial evolution of Cenozoic extension in the eastern part of the Pyrenees as well as the potential driving mechanisms for this evolution.

2. Geological Setting

2.1. Tectonic Evolution of the Eastern Part of the Pyrenees

The Pyrenees result from the North-South convergence of the Eurasian and Iberian plates since the late Cretaceous (Beaumont et al., 2000; Choukroune, 1989; Mouthereau et al., 2014; Muñoz, 1992; Roure et al., 1989; Teixell et al., 2016), and form a double-wedged mountain range of around 1,000 km long and 150 km wide (Figure 1a). The maximum of shortening occurred during the Eocene in the central part of the range (e.g., Curry et al., 2019; Fillon & van der Beek, 2012; Gibson et al., 2007; Metcalf et al., 2009; Mouthereau et al., 2014; Sinclair et al., 2005; Teixell et al., 2016; Vergés et al., 1995; Whitchurch et al., 2011). The Pyrenees are divided into three main latitudinal tectonostratigraphic domains (Grool et al., 2018; Vergés et al., 2002). To the North, three main units are recognized: the Aquitaine foreland basin, the Sub Pyrenean Zone, and the North Pyrenean Zone, the last two being separated by the North Pyrenean Frontal Thrust (Figure 1a). Further South, the North Pyrenean Fault (NPF) separates the North Pyrenean Zone from the Axial Zone and is interpreted as the suture between the Eurasian and Iberian plates. The Axial Zone consists of a stack of south-verging nappes made of late Proterozoic and Paleozoic sedimentary, metamorphic, and magmatic rocks involved in the Variscan orogeny. The South Pyrenean Zone extends to the South of the Axial Zone and is composed of a sequence of Mesozoic to Eocene sediments involved in several thrust sheets transported southward. The Ebro basin forms the southern foreland basin of the Pyrenean orogen.

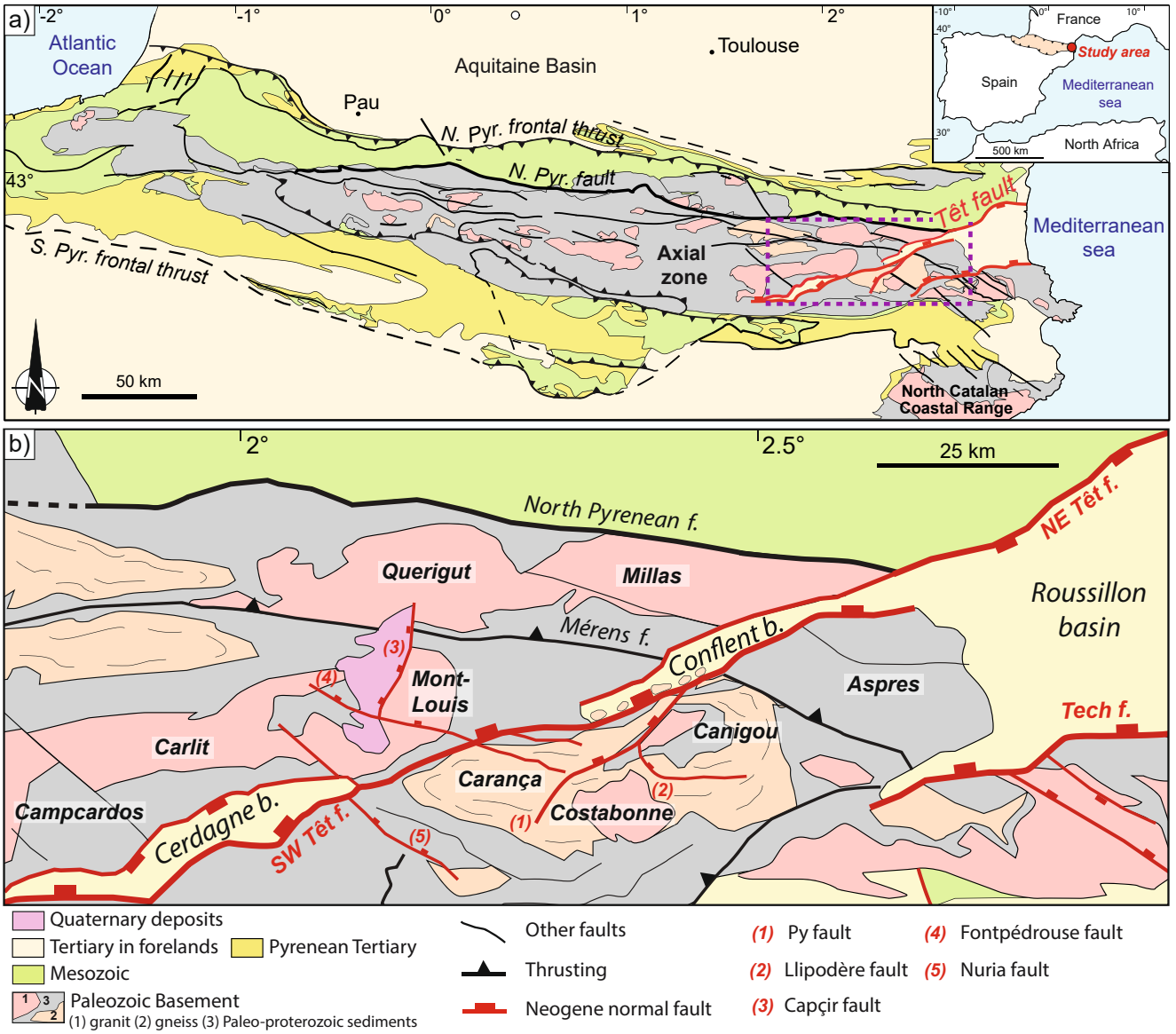

Figure 1. (a) Structural map of the Pyrenees showing the main structural domains delimited by faults (modified after Taillefer et al., 2017). The major Neogene normal faults of the Eastern Pyrenees are reported in red. The study area is outlined with an open purple-dashed box. (b) Structural sketch map of the study area showing the different massifs (in bold italics) and basins (in italics) along the Southwestern (SW) and Northeastern (NE) segments of the Têt fault (modified from Taillefer et al., 2021). Secondary faults are indicated by red numbers (see legend for details).

In the eastern Axial Zone, it is accepted that the mountain building occurred through the emplacement of south-verging nappes rooted in the northern part of the Axial Zone, south of the NPF (Laumonier et al., 2015; Sibuet et al., 2004; Vergés et al., 1995; Teixell et al., 2016). In the studied area, the balanced cross-sections of Ternois et al. (2019) suggest an Eocene thrusting of the Aspres-Mont-Louis massifs onto the Canigou massif, in agreement with available thermochronological data (Maurel et al., 2008). The reactivation of Variscan structures during the Pyrenean orogeny has been proposed, the most significant example being the Merens fault to the North of our study area (Burbank et al., 1992; Cochelin et al., 2017; Guitard et al., 1998; Laumonier et al., 2017; McCaig & Miller, 1986). The particularity of the Eastern Pyrenees is the reactivation of compressional structures during extensional tectonic regime (Calvet et al., 2021; Jolivet et al., 2020; Séranne, 1999; Séranne et al., 1995, 2021). This regional scale extension is witnessed by geophysical data that show a progressive crustal thinning, with crustal thickness varying between 45 km in the eastern part of the Axial Zone (~1°E) to 25 km at the margin of the Gulf of Lion (Chevrot et al., 2018; Diaz et al., 2018). This regional extensional episode led to the (re-)activation

of major structures as normal faults with different orientations (NE-SW, NW-SE, and N-S, Figure 1b), from the end of the Oligocene to the Quaternary (Taillefer et al., 2021). Some of these faults have been considered as inherited ductile Variscan faults (Autran et al., 2005; Bouchez & Gleizes, 1995; Guitard et al., 1992, 1998; Laumonier et al., 2015, 2017). Two main NE-SW trending normal faults are recognized in the studied area: the Têt and the Tech faults (Figure 1b). The Têt fault represents the southern margin of the Cerdagne and Conflent basins, while the Tech fault is the southern bounding fault of the Roussillon basin. Noteworthy is the importance of an NW-SE trending fault network that affects particularly the Mont-Louis and Carança massifs (e.g., Fontpédrouse and Nuria faults, Figure 1b) and cuts the North Catalan Coastal Range further South (Figure 1a). Some of these faults have nearly E-W directions probably recording spatial and/or temporal changes of stress orientation and/or stress regime. Major N-S faults in the eastern part of the Pyrenees are rare, among which the Capçir fault is described as a Quaternary normal fault (Briais et al., 1990). In the study area, the kinematics and amount of exhumation associated to these different faults are still debated. In Figure 1b, major crustal blocks have been differentiated and delimited by the Têt fault, namely the Mont-Louis block to the North (hanging wall) and Canigou-Costabonne and Carança blocks (footwall, delimited by the Py secondary fault) to the South.

Previous multi-thermochronological studies (Gunnell et al., 2009; Maurel et al., 2002, 2008) in the Canigou (footwall of the Têt fault) and Mont-Louis (hanging wall of the Têt fault) provided insights and results guiding our study. Maurel et al. (2002, 2008) proposed that the Canigou massif was exhumed during two periods, the first one at a rate of ∼0.30 km/Ma between 27 and 21 Ma, followed by a significant slowdown of exhumation (∼0.10 km/Ma) until present-day. In the Mont-Louis massif, thermochronological data suggest an earlier exhumation between 50 and 35 Ma (∼0.30 km/Ma) accompanied by a rapid cooling. Since 35 Ma, the Mont Louis exhumation has been relatively slow, estimated at 0.04–0.06 km/Ma (Maurel et al., 2008). These different exhumation and cooling histories between the two massifs since 35 Ma were interpreted to be related to the normal motion of the Têt fault, without erasing the thermochronological record of Eocene tectonic activity in the hanging wall. In the Carança massif, thermal modeling based on AHe data (Milesi, Monié, Münch, et al., 2020; Milesi et al., 2019) suggests two main cooling events that occurred in the Oligo-Miocene, a major one between 30 and 24 Ma (at a rate of 25°C/Ma) followed by a second episode between 12 and 9 Ma (at a rate of 15°C/Ma). Despite these previous thermochrological studies, the spatio-temporal evolution of the main tectonic structures in the eastern part of the Axial Zone of the Pyrenees since the Priabonian remains still poorly constrained (see Taillefer et al., 2021).

2.2. Tectonic Evolution and Sedimentary Record Along the Têt Fault

The southern segment of the Têt normal fault is a NE-SW north-dipping and 100 km long crustal-scale fault (Chevrot et al., 2018; Diaz et al., 2018; Maurel et al., 2002, 2008; Figure 1a). It crosscuts Palaeozoic magmatic and metamorphic rocks of the Mont Louis, Canigou, and Carança massifs along which Neogene sedimentary basins developed (Figure 1b). In the Canigou massif, the main period of fault activity during the Oligo-Miocene has been well constrained using low-T thermochronology (Maurel et al., 2002, 2008). A second stage of normal motion along the entire Têt fault has been recorded between the Middle-Miocene and the late Pliocene, with associated vertical displacements in the range of 150–500 m (Agustí et al., 2006; Cabrera et al., 1988; Calvet, 1999; Carozza & Baize, 2004; Clauzon et al., 2015; Delcaillau et al., 2004; Pous et al., 1986; Réhault et al., 1987; Roca & Desegaulx, 1992; Tassone et al., 1994) to kilometric (Calvet, 1996). However, thermochronological data in the Canigou massif (Maurel et al., 2008) are apparently not consistent with a hypothesis of km-scale vertical displacements. Since the end of Miocene, a main difference is recorded along the Têt fault between the western (Cerdagne basin) and eastern (Conflent and Roussillon basins) segments. Indeed, only the western segment of the Têt fault has been active (Calvet, 1999) which led to the opening of the Cerdagne pull-apart basin accommodated by normal (Agustí et al., 2006; Pous et al., 1986) and right-lateral displacement along the Têt fault (Cabrera et al., 1988). Based on geomorphological observations, a westward propagation of the deformation along the Têt fault has also been proposed to occur during the Plio-Pleistocene (Carozza & Baize, 2004; Carozza & Delcaillau, 1999). The amplitude of Pliocene to Quaternary normal activity on the eastern segment of the Têt fault is still debated. For some authors, the presence of triangular facet. along the Têt fault scarp documents a recent normal fault activity (Briais et al., 1990; Calvet, 1999). However, Petit and Mouthereau (2012) suggested these are only the morphological expression of the differential erosion within Variscan mylonites. It is important to note that facets are also observed on scarps with no apparent mylonite nor favorably oriented Variscan foliation (western segment of the Têt fault, Py, and Capcir faults, Delmas et al., 2018). Finally, over the last 6 Ma, low incision rates

of maximum 25 m/Ma in the Têt valley indicate weak vertical uplift in the study area (Sartégou et al., 2018), bringing further evidence to the ongoing discussion on late-Miocene potential uplift from paleoelevation studies (Huyghe et al., 2020; Suc & Fauquette, 2012).

The sedimentary record is not continuous along the Têt fault system, and three main depositional areas can be distinguished from East to West: (a) the Roussillon basin bounded to the North by the northern segment of the Têt fault that is antithetic to the southern segment, (b) the Conflent basin that connects to the Roussillon basin to the East and (c) the Cerdagne basin along the southwestern segment of the Têt fault (Figure 1b). The Roussillon basin is a large graben belonging to the West European Rift system and was highly subsident during the Oligocene-Aquitanian interval that corresponds to the rifting phase preluding the Liguro-Provencal Sea opening. Post-rift deposits within the Roussillon basin were deposited in a passive margin geotectonic setting with low tectonic subsidence, and were deeply incised during the Messinian salinity crisis after which the passive margin sedimentation resumed during the Pliocene (Calvet et al., 2015, 2021; Clauzon, 1990; Clauzon et al., 1987). The Conflent basin is an intramontane half-graben lying along the southwestern segment of the Têt fault, at an elevation ranging from 250 to 1,000 m. Its sedimentary infill is composed of up to ∼1,000 m thick continental deposits, thought to be related to the main tectonic activity of the Têt fault (Calvet et al., 2014; Guitard et al., 1998). However, the stratigraphy of this basin is debated and the main sedimentary units, peculiarly an olistostrome with km-scale olistoliths originated from the Canigou massif, may be either early Burdigalian (Calvet et al., 2014; Guitard et al., 1998) or Pliocene (Clauzon et al., 2015). Toward the southwest, the Cerdagne basin, at an elevation of 1,100 m, is interpreted as a pull-apart basin formed by dextral-strike slip along the Têt fault (Cabrera et al., 1988). It has been infilled by 400–1,000 m of Neogene sediments divided into two depositional units from early Miocene and late Miocene, separated by an unconformity (Agustí & Roca, 1987; Cabrera et al., 1988; Pous et al., 1986; Roca, 1996). The source area of clastic sediments switched from the North to the South between these two units, with tectonic activity strongly decreasing during the late Miocene (Cabrera et al., 1988; Roca & Santanach, 1986).

3. Methodology

3.1. Low-Temperature Thermochronology

3.1.1. Sampling Strategy

Our main objective is to quantify the exhumation and thermal evolution of the different crustal blocks separated by main regional faults, and to provide new data on the kinematic history of these faults. In the hanging wall of the Têt fault, two main blocks, separated by the Mérens fault, have been studied: respectively the North and South Mérens blocks. The North Mérens block is composed of the Millas and Querigut granitic massifs, and the South Mérens block is formed by Mont-Louis, Campcardos and Carlit massifs (Figure 1b). In the footwall of the Têt fault, two main blocks, separated by the NE-SW trending Py fault, have been sampled: the Canigou-Costabonne block (eastern segment of the Têt fault, Canigou and Costabonne sub-blocks separated by the NW-SE Llipodère fault) and the Carança block (western segment). New AHe, AFT, and ZHe ages have been obtained mainly in the footwall of the Têt fault (Carança and Canigou-Costabonne blocks), which represents a total of 44 AHe ages, 3 AFT ages, and 25 ZHe ages (Tables 1 and 2). Thermochronological data from previous studies (Gunnell et al., 2009; Maurel et al., 2008) have been synthetized and supplemented by AHe ages from our previous studies (Milesi, Monié, Münch, et al., 2020; Milesi et al., 2019). Note that we have excluded samples affected by hydrothermalism and Rare Earth Element mobility, therefore not relevant to define regional exhumation and thermal evolution of the studied area (Milesi, Monié, Münch, et al., 2020; Milesi et al., 2019, Figure 2). Sample localities and corresponding thermochronological data from literature are summarized in Table S1 in Supporting Information S1 and shown in Figure 2.

In the hanging wall of the Têt fault, six samples at an elevation between 730 and 2,380 m were analyzed in the North Mérens block (DON, MAD, and MTB). The South Mérens block (i.e., Mont-Louis massif) provided 17 samples (CAR, CMPC, GAL, LPCH, ML, ST) with an elevation difference of ∼1,800 m between the lowest sample in the Têt Valley (1,081 m) and that of the summit of Campcardos (2,900 m). In the footwall of the Têt fault, the Costabonne massif includes four samples (GUIL and POMA) from Gunnell et al. (2009) and two samples (VER) dated in this study. In the Canigou massif, Maurel et al. (2008) reported thermochronological data on seven samples (CAN) collected along a profile from the base of the massif (970 m) to the

Table 1
(U-Th)/He Data on Apatite and Zircon

Block	Sample/ grain	Rs µm	U ppm	Th Ppm	eU ppm	Th/U	4He ncc/g	± s ncc/g	Ft	Corrected age Ma	Error ±1σ (Ma)
						Apatite					
South Mérens block	**ST13** (42.50727N 2.15867E 1,289m) Augen gneiss										
	ST13a	81.8	12.4	18.6	16.9	1.5	29023.1	1160.9	0.84	17.0	0.8
	ST13b	81.3	14.1	16.0	17.9	1.1	28315.3	849.5	0.85	15.5	0.6
	ST13c	67.0	24.2	24.4	30.0	1.0	49313.1	986.3	0.82	16.7	0.7
	ST13d	59.9	14.3	14.6	17.8	1.0	30276.5	1211.1	0.82	17.2	0.7
	ST13e	61.3	77.2	73.7	94.9	1.0	143789.9	1437.9	0.82	15.4	0.7
	ST13f	45.5	48.5	59.8	62.9	1.2	102885.4	2057.7	0.7	18.1	0.8
	*ST13g**	*53.3*	*130.3*	*158.8*	*168.4*	*1.2*	*356975.6*	*3569.8*	*0.8*	*22.9*	*1.0*
	*ST13h**	*43.9*	*94.3*	*102.8*	*119.0*	*1.1*	*227047.7*	*2951.6*	*0.7*	*21.9*	*1.1*
									Mean	**16.7**	**1.0**
Carança block	**GAL5** (42.51287N 2.20037E 1,147m) Granite										
	GAL5a	57.3	20.6	5.1	21.8	0.2	19915.4	597.5	0.77	9.8	0.6
	GAL5b	62.7	11.2	5.6	12.5	0.5	15730.0	471.9	0.81	12.9	0.8
	GAL5c	60.8	7.8	2.1	8.4	0.3	10375.3	415.0	0.79	13.0	0.8
									Mean	**11.9**	**1.8**
	ST10 (42.4949N 2.17104E 1,383m) Augen gneiss										
	ST10a	61.3	50.1	28.0	56.8	0.6	109832.3	2196.6	0.77	20.9	1.2
	ST10b	56.3	62.3	27.3	68.8	0.4	94741.0	1136.9	0.75	15.3	0.8
	ST10c	75.1	56.1	26.4	62.4	0.5	103165.4	1547.5	0.81	17.0	0.9
	ST10d	67.0	29.1	7.4	30.8	0.3	76314.5	1526.3	0.81	25.2	1.3
									Mean	**19.6**	**4.4**
	ST9 (42.49203N 2.17351E 1,421m) Fractured augen gneiss										
	ST9a	60.4	46.6	17.7	50.8	0.4	119148.9	1191.5	0.79	24.7	1.2
	ST9b	68.1	38.6	10.2	41.0	0.3	83334.3	1666.7	0.83	20.4	1.0
	ST9c	68.0	59.8	25.8	66.0	0.4	158824.9	1588.2	0.81	24.5	1.3
	ST9d	63.2	54.0	19.8	58.8	0.4	164830.2	1648.3	0.84	27.8	1.7
									Mean	**24.3**	**3.0**
	ST7 (42.48421N 2.17433E 1,494m) Augen gneiss										
	ST7a	61.0	11.3	3.2	12.1	0.3	18475.0	923.8	0.79	16.1	0.8
	ST7b	64.6	16.1	4.6	17.2	0.3	31125.3	1245.0	0.80	18.7	0.9
	ST7c	70.5	24.1	5.9	25.5	0.2	40022.5	800.4	0.82	15.8	0.7
	ST7d	63.5	14.2	3.7	15.1	0.3	26010.2	1040.4	0.80	17.9	0.9
									Mean	**17.1**	**1.4**
	ST6 (42.48116N 2.17433E 1,533m) Augen gneiss										
	ST6a	82.1	7.4	2.6	8.1	0.4	27252.5	817.6	0.85	33.1	1.8
	ST6b	62.3	13.1	3.3	13.9	0.3	28447.2	1137.9	0.78	21.7	1.1
	ST6c	67.9	7.2	3.3	8.0	0.5	17354.2	867.7	0.82	21.9	1.0
									Mean	**25.5**	**6.5**

Table 1
Continued

Block	Sample/ grain	Rs µm	U ppm	Th Ppm	eU ppm	Th/U	4He ncc/g	± s ncc/g	Ft	Corrected age Ma	Error ±1σ (Ma)
Canigou block	**CAN12** (42.56647N 2.48237E 970m) Augen gneiss										
	CAN12a	77.8	32.7	17.4	36.9	0.5	67808.4	678.1	0.84	18.1	0.9
	CAN12b	61.3	32.4	10.6	35.0	0.3	54050.7	540.5	0.83	15.5	0.7
	CAN12c	102.6	8.3	24.1	14.1	2.9	25356.0	253.6	0.90	16.6	0.8
									Mean	**16.7**	**1.3**
	CAN8 (42.53956N 2.46652E 2,050m) Augen gneiss										
	CAN8a	80	33.5	2.4	34.1	0.1	67878.1	678.8	0.84	19.6	1.0
	CAN4 (42.51892N 2.45676E 2,784m) Augen gneiss										
	CAN4a	42.6	8.1	17.9	12.4	2.2	25850.1	258.5	0.71	24.3	1.5
	CAN4b	45.1	16.5	43.7	27.0	2.6	62074.6	620.7	0.74	26.0	1.4
	CAN4c	61.7	11.6	35.4	20.1	3.0	64660.9	646.6	0.80	33.5	1.9
									Mean	**27.9**	**4.8**
Costabonne block	**VER11** (42.477943N 2.305973E 1,560m) Highly fractured augen gneiss with chlorite										
	VER11a	50.0	237.6	17.0	241.7	0.1	639343.3	6393.4	0.75	29.2	1.4
	VER11b	47.9	228.1	19.4	232.7	0.1	684958.3	6849.6	0.74	32.7	1.6
	VER11c	49.9	153.7	13.2	156.9	0.1	429612.5	4296.1	0.76	29.9	1.5
									Mean	**30.6**	**1.8**
	VER13 (42.471203N 2.343885E 1,935m) Augen gneiss										
	*VER13a**	*61.9*	*377.9*	*156.1*	*415.3*	*0.4*	*969933.9*	*9699.3*	*0.81*	*24.0*	*1.3*
	VER13b	52.9	275.0	61.6	289.8	0.2	920151.0	9201.5	0.77	34.3	1.8
	VER13c	57.7	237.9	65.3	253.6	0.3	860128.9	8601.3	0.79	35.4	1.8
									Mean	**34.9**	**1.8**
Olistolithes	**OL2** (42.55702N 2.39468E 780m) Fractured augen gneiss										
	OL2a	81.2	15.2	9.2	17.4	0.6	76552.5	765.5	0.85	43.1	2.0
	OL2b	38.6	41.7	49.8	53.7	1.2	100135.0	1001.4	0.71	21.7	1.1
	OL2c	82.5	13.0	16.3	16.9	1.3	87438.1	874.4	0.87	49.5	2.2
	OL1 (42.53754N 2.3375E 930m) Fractured augen gneiss										
	OL1a	48.4	17.2	10.7	19.7	0.6	72121.3	721.2	0.71	42.9	2.4
	OL1b	56.7	20.9	9.7	23.2	0.5	88868.5	888.7	0.78	40.8	2.3
						Zircon					
Carança block	**TET1.1** (42.52611N 2.24305555E 900 m) Granite with chlorite										
	TET1.1a	47.9	1185.3	530.6	1312.6	0.4	2188733.2	43774.7	0.70	19.7	1.6
	TET1.1b	71.0	632.9	201.8	681.3	0.3	1577103.0	41004.7	0.80	23.9	1.9
	TET1.1c	53.5	525.5	215.5	577.2	0.4	1158414.3	20851.5	0.77	21.6	1.7
	TET1.1d	54.7	581.0	338.7	662.3	0.6	1397788.4	29353.6	0.77	22.7	1.8
									Mean	**22.0**	**1.7**

Table 1
Continued

Block	Sample/ grain	Rs µm	U ppm	Th Ppm	eU ppm	Th/U	4He ncc/g	± s ncc/g	Ft	Corrected age Ma	Error ±1σ (Ma)
	TET4 (42.51175N 2.25487E 1,390m) Augen gneiss										
	TET4a	73.7	460.9	175.7	503.0	0.4	1449839.5	21747.6	0.83	28.7	2.3
	TET4b	60.8	548.1	770.2	733.0	1.4	2244859.4	24693.5	0.76	33.5	2.7
	TET4c	56.1	869.6	320.0	946.4	0.4	3000148.0	48002.4	0.75	35.2	2.8
									Mean	**32.5**	**3.3**
	TET5 (42.49078N 2.23036E 1,900m) Augen Gneiss										
	TET5a	63.7	564.0	149.9	600.0	0.3	2172324.1	39101.8	0.77	38.9	3.1
	TET5b	67.8	933.1	423.6	1034.8	0.5	3586410.1	71728.2	0.79	36.3	2.9
	TET5c	68.5	1192.0	315.4	1267.7	0.3	4567608.3	68514.1	0.82	36.4	2.9
	TET5d	58.9	968.6	452.4	1077.1	0.5	3262406.1	48936.1	0.76	33.2	2.7
									Mean	**36.2**	**2.9**
	GAL7 (42.51505N 2.19904E 1,025m) Fractured fine grained gneiss with quartz and calcite veins and locally oxides										
	GAL7a	62.4	1090.8	483.6	1206.8	0.4	2620687.7	39310.3	0.80	22.4	1.8
	GAL7b	54.7	950.0	407.1	1047.7	0.4	2191714.2	39450.9	0.74	23.5	1.9
	GAL7c	52.3	1264.8	556.2	1398.3	0.4	3105604.0	52795.3	0.77	24.0	1.9
									Mean	**23.3**	**1.9**
	GAL3 (42.51018N 2.20525E 1,363m) Fine grained gneiss										
	GAL3a	55.4	1678.1	328.7	1757.0	0.2	4976741.5	59720.9	0.74	31.6	2.5
	GAL3b	59.8	685.1	436.9	789.9	0.6	2120801.6	31812.0	0.78	28.6	2.3
	GAL3c	67.4	685.6	477.6	800.3	0.7	2144053.6	40737.0	0.81	27.5	2.2
	GAL3d	66.0	881.9	207.1	931.6	0.2	2581295.1	41300.7	0.78	29.4	2.3
									Mean	**29.3**	**2.3**
	ST3 (42.50001N 2.16697E 1,174m) Unaltered gneiss with biotite										
	ST3a	59.9	1316.3	557.5	1450.2	0.4	3801126.6	49414.6	0.76	28.6	2.3
	ST3b	63.4	1802.8	314.4	1878.2	0.2	4910004.5	68740.1	0.77	28.0	2.2
	ST3c	61.3	1121.4	661.1	1280.0	0.6	2993707.8	47899.3	0.77	25.3	2.0
									Mean	**27.3**	**2.2**
	PLA3 (42.49343N 2.15462E 1,622 m) Fractured leucocratic gneiss and locally oxidized										
	PLA3a	49.5	2958.1	226.3	3012.4	0.1	9898474.3	89086.3	0.75	36.2	2.9
	PLA3b	50.4	3478.6	417.7	3578.8	0.1	11888683.1	106998.1	0.75	36.8	2.9
	PLA3c	61.3	1678.8	277.0	1745.2	0.2	6282251.9	50258.0	0.77	38.9	3.1
									Mean	**37.3**	**3.0**

Note. Ft: Alpha ejection correction (Farley et al., 1996)

summit (2,784 m). Three apatite samples (CAN4, CAN9, and CAN12), initially dated with the AHe population method, have been redated with AHe single grain method (see Section 3.1.2). Two augen gneiss blocks (OL1 and OL2) from the olistostrome formation deposited in the Conflent basin and originating from the Canigou massif (Clauzon et al., 2015) have been also dated with the AHe single-grain method. In the Carança block, five new samples have been dated with the AHe method (GAL5, ST6, ST7, ST9, and ST10) to complete the AHe data set from Milesi, Monié, Münch, et al. (2020) and Milesi et al. (2019). AFT ages have been obtained on three samples from different sampling profiles (ST2, GAL4, and TET4). Finally, a ZHe age-elevation profile (900–1,900 m) has been realized with six samples from the Carança block (TET1.1, TET4, TET5, GAL7, GAL3, PLA3, and ST3).

Table 2
Fission Track Data for the Carança Massif

Sample (elevation)	No. of crystals	Track density (x106 tr.cm-2) ρd[Nd]	ρs[Ns]	ρi[Ni]	Age dispersion RE (%)	$P\chi^2$ (%)	U(ppm)	Central age (Ma ± 1σ)	Mean track length (μm)	StD (μm)	No. of tracks measured
TET4	10	1.183	0.400	4.546	0.1	67.37	48.0	17.4 ± 1,7	12.84 ± 0.5	1.81	35
1,390 m		[10,391]	[119]	[1,377]							
GAL4	16	1.189	0.333	4.659	14.7	17.14	49.0	15.20 ± 1.4	12.81 ± 0.7	2.53	40
1,221 m		[10,391]	[163]	[2,203]							
ST2	20	1.177	0.307	3.601	17.6	28.01	38.3	17.4 ± 1.7	12.39 ± 0.5	2.46	57
1,217 m		[10,391]	[150]	[1741]							

Note. Analyses were determined by the external detector method using 0.5 for the $4\pi/2\pi$ geometry correction factor. Apatite fission track ages were calculated using dosimeter glass (CN-5; Analyst Stephanie Brichau, $\xi = 341.8 \pm 7.8$) calibrated by multiple analyses of IUGS apatite age standards (Hurford, 1990). $P\chi^2$ is probability of obtaining χ^2 value for v degrees of freedom, where v is the amount of crystals. Central age is a modal age, weighted for different precisions of individual crystals. In track density, ρd is the fission track density of the standard U-glass (CN-5); Ns (spontaneous), Ni (induced) and Nd (dosemeter) are the fission track numbers corresponding to ρs, ρi, and ρd, respectively.

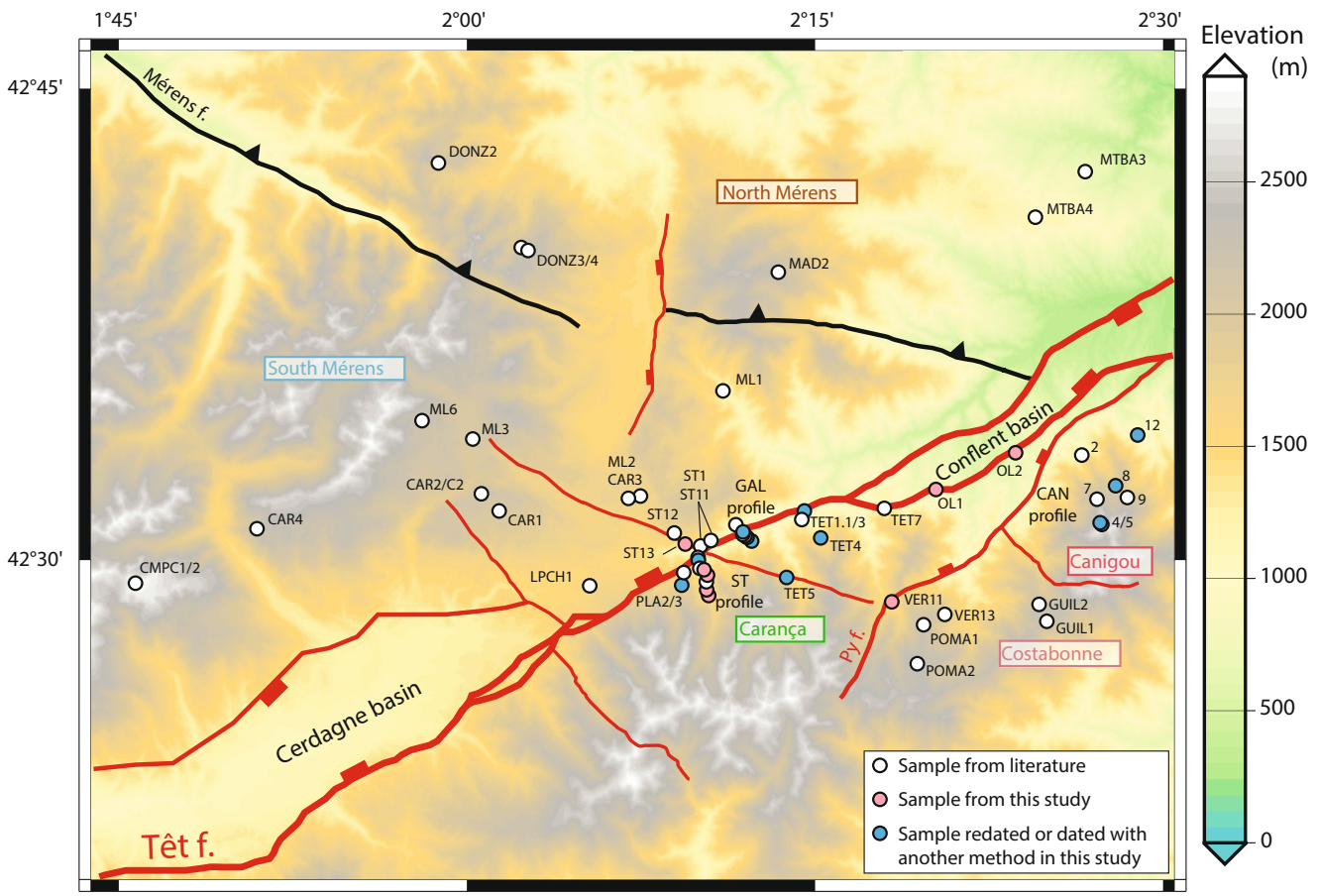

Figure 2. Location of samples projected on DEM under GMT (Wessel et al., 2019) using SRTM1s. Different crustal blocks are delimited by regional major faults. From the North to the South, the sample names are for ST profile: ST2, ST3, ST4, ST10, ST9, ST8, ST7, ST6 and for GAL profile: GAL7, GAL6, GAL5, GAL4, GAL3, and GAL1. Samples ST2, ST6, ST7, ST9, ST10, GAL4, and GAL5 were dated in this study.

3.1.2. Apatite and Zircon (U-Th)/He Dating

Apatite and zircon (U-Th)/He analyses were conducted at the Noble Gas Laboratory of Géosciences Montpellier (France). All samples were crushed and sieved, and apatite and zircon concentrates were obtained by heavy liquid methods. Inclusion-free crystals with no evidence of fracture were hand-picked under a binocular microscope. Each single grain was packed in Pt tubes for apatite or Nb tube for zircon, placed under vacuum, and heated with a 1,090 nm fiber laser operating at 4.0 W (900°C) for apatite and 6.2 W (1,100°C) for zircon. We applied a duration of heating of 5 min for apatite and 15 min for zircon. After ^{3}He spiking, gas purification was achieved by a cryogenic trap and two SAES AP-10-N getters, and helium content was measured on a quadrupole Prisma-Plus QMG 220. The ^{4}He content was determined by the peak height method and was 10–10,000 times above typical blank levels. A second heating run using the same analytical procedure was systematically conducted to verify that more than 99% of ^{4}He was extracted during the first run. After helium extraction, Pt or Nb tubes were retrieved from the sample chamber and transferred in a 2 ml polypropylene conical tube. Samples were doubly spiked (^{230}Th and ^{233}U) and dissolved using procedures previously described by Wu et al. (2016) for apatite and Gautheron et al. (2021) for zircon. The resulting solutions were diluted, and U (^{233}U and ^{238}U) and Th (^{230}Th and ^{232}Th) were measured by using isotope dilution ICPMS. For age calculation, alpha ejection correction (Farley et al., 1996) was calculated using the Ft software (Gautheron & Tassan-Got, 2010; Ketcham et al., 2011). Durango apatite and Fish Canyon Tuff (FCT) zircon replicates were analyzed between four unknown grains and yielded a mean age of 31.24 ± 2.18 and 29.19 ± 1.19 Ma, respectively, during the different analyses of this study. These results are consistent with the Durango reference age of 31.02 ± 1.01 Ma given by McDowell et al. (2005) and FCT reference age of 28.30 ± 2.8 Ma (Reiners & Nicolescu, 2006). Conservatively, the He partial retention zone for the zircon system is assumed to be between 140°C and 220°C (Guenthner et al., 2013) and in the range of 40°C–80°C for apatite (Stockli et al., 2000). It is important to note that the helium retention is sensitive to the crystal chemistry (eU values, chlorine content) and cooling history of samples (see Ault et al., 2019), and also that the PRZ can spread over a larger range of temperature (see Ault et al., 2019).

3.1.3. Apatite Fission Tracks

Apatite grains were mounted and polished for etching to reveal the natural spontaneous fission tracks. Apatites were etched using 5.5N HNO3 at 20°C for 20 s. Etched grain mounts were packed with mica external detectors and corning glass (CN5) dosimeters and irradiated in the Chilean CCHEN nuclear reactor. Following irradiation, the external detectors were etched using 40% HF at 20°C for 40 min. Analyses were carried out on an Olympus BX61 microscope at a magnification of ×1,250, using a dry (×100) objective in the Dating laboratory of Géosciences Environnement Toulouse (France). Confined track-length measurements were performed using a drawing tube and digitizing tablet, calibrated against a stage micrometer. Single-grain AFT ages were calculated using the external detector method and the zeta calibration approach, as recommended by the I.U.G.S. Subcommission on Geochronology (Hurford, 1990). Track-length measurements were restricted to confined tracks parallel to the c-crystallographic axis. Fission tracks in apatite shorten or anneal with increased temperature and duration of heating. For apatite of typical Durango composition (0.4 wt% Cl), experimental and borehole data (Green et al., 1989; Ketcham et al., 1999) show that over geologic time fission tracks begin to anneal at a sufficient rate to be measurable above ∼60°C, with complete annealing and total resetting of the AFT age occurring between 100°C and 120°C. This range of temperatures is usually labeled the apatite fission track partial annealing zone (PAZ).

3.2. Thermochronological Data Interpretation

3.2.1. Age-Elevation Relationships (AER)

For each crustal block (Figure 2), the AERs between the different thermochronological data have been used to estimate first-order apparent exhumation rates and also to get information on timing for potential changes in exhumation (i.e., break-in-slope in AERs). This approach is independent from the thermal structure of the block under consideration (e.g., Braun, 2002; Fitzgerald & Malusà, 2019; Fitzgerald et al., 1995; Wagner et al., 1977), but it relies on several assumptions and simplifications. First, it only considers the measured thermochronological ages without taking into account potential sample-specific kinetics from parent element content for instance (e.g., Ault et al., 2019). The AER approach also considers a vertical distribution of investigated samples (Stüwe et al., 1994), which is rarely the case in the field, and may also be influenced by potential changes in topography

(Braun, 2002) or the presence of secondary faults. A major potential problem concerning the interpretation of AERs is the complexity of the exhumation scenario (i.e., number of segments which can be defined in an age-elevation data set), we thus used a Bayesian Information Criterion (BIC) to select the appropriate model complexity (Schwarz, 1978). In this study, we followed the approach developed by Glotzbach et al. (2011) to determine the best-fitting AER estimates for AHe, AFT, and ZHe data with minimization of the BIC.

3.2.2. Inverse Thermal Modeling Under QTQt

In order to reconstruct the thermal history of the different crustal blocks (Figure 2), time-temperature paths were modeled with QTQt 5.7.0 software (Gallagher, 2012; Gallagher et al., 2009) using AHe and ZHe single-grain ages and parameters (eU, Rs) together with AFT single-grain ages with length distribution data. QTQt software uses a Bayesian Markov chain Monte Carlo sampling method to infer sample time-temperature histories (Charvin et al., 2009; Sambridge, 1999). This software is particularly efficient to model together several samples from the same elevation profile. We parametrized modeling to allow all samples of a given elevation profile to evolve under a common thermal path with a typical geothermal gradient of 30°C ± 10°C in order to take full advantage of the multi-sample inversion approach (Vermeesch & Tian, 2014). The radiation-damage model of Gautheron et al. (2009) has been chosen for the AHe, the kinetic models of Ketcham et al. (2007) for AFT and Guenthner et al. (2013) diffusion model for ZHe. For each model, 100,000 iterations have been performed and the predicted vs. observed ages graph is systematically presented with output time-temperature histories. ZHe data are modeled only for the Carança block (where we obtained a ZHe elevation profile), and are used as first-order time-temperature constraints to define the thermal histories of the other crustal blocks (no available ZHe profile, only scarce individual data obtained with the population method).

4. Results

4.1. New Thermochronological Ages

4.1.1. Apatite and Zircon (U-Th)/He

All AHe and ZHe single-grain ages obtained in this study are reported in Table 1. We also present different graphs of ages vs. Rs, eU, and Th/U in the Supporting Information (Figure S1 in Supporting Information S1). For the South Mérens block, an augen gneiss (sample ST13) was collected in the footwall of the Fontpédrouse fault and provides a mean AHe age of 16.7 ± 1.0 Ma. Two apatite grains have not been considered to calculate the mean AHe age due to their anomalous high eU content compared to the other grains, possibly due to U-rich inclusions in these apatite grains (Table 2 and Figure S1 in Supporting Information S1). Note that ST13 has an AHe age younger than all AHe ages (all >25 Ma) previously obtained in the South Mérens block (Maurel et al., 2008; Milesi, Monié, Münch, et al., 2020). This cannot be explained by different Rs or eU values of the dated apatite grains (Table 1, Figure S1 in Supporting Information S1) and therefore sample ST13 will be considered independently of other samples from the South Mérens block due to its particular structural position in the footwall of the Fontpédrouse fault (Figure 3).

In the footwall of the Têt fault, three samples from the Canigou massif, previously analyzed using multigrain AHe approach, were re-processed using a single-grain approach. Sample CAN12 from the base of the profile (970 m) shows a mean AHe age of 16.7 ± 1.3 Ma that agrees with the multigrain AHe age of 18.8 ± 1.0 Ma (Maurel et al., 2008). On top of the massif (2,784 m), sample CAN4 displays larger single-grain AHe age dispersion between 24.3 and 33.5 Ma, without any clear relationship with the apatite chemical composition (Table 1 and Figure S1 in Supporting Information S1). The mean single-grain AHe age of CAN4 (27.9 ± 4.8 Ma), despite high uncertainty, is younger than the multigrain AHe age of 34.7 ± 1.7 Ma obtained on three aliquots by Maurel et al. (2008). At an intermediate elevation (2,050 m), a single apatite grain provides an AHe age of 19.6 ± 1.0 Ma for sample CAN8. In the southern Costabonne massif, two samples VER11 (1,560 m) and VER13 (1,935 m) show low intra-sample age dispersion, except one apatite grain excluded for the mean age calculation due to its important eU content and young AHe age (Table 1 and Figure S1 in Supporting Information S1). AHe ages are respectively of 30.6 ± 1.8 Ma for VER11 and 34.9 ± 1.8 Ma for VER13. In the olistostrome of the Conflent basin, two augen gneisses (OL1 and OL2, Figure 2) provide five AHe ages with four of them between 40.8 ± 2.3 and 49.5 ± 2.2 Ma, and one at 21.7 ± 1.1 Ma. In the Carança massif, a new AHe mean age of 11.9 ± 0.9 Ma has been obtained for a granite sample (GAL5), thus confirming the previous single-grain AHe ages between 10.0 ± 0.4 and 14.1 ± 1.1 Ma obtained for the GAL profile (Milesi, Monié, Münch, et al., 2020). In the western

part of Carança block, samples ST6, ST7, ST9, and ST10 collected at a similar elevation provide mean AHe ages of 25.5 ± 6.5, 17.1 ± 1.4, 24.3 ± 3.0, and 19.6 ± 4.4 Ma, respectively (Table 1 and Figure 3). ST samples provide quite large intra-sample variability in AHe ages, which cannot be explained by the chemical characteristics (eU, Th/U) or the grain size (Rs).

In the Carança massif, seven samples collected at different elevations (from 900 to 1,900 m) have been dated using the single-grain ZHe method. These zircon grains have an eU content mostly ranging between 500 and 1,900 ppm, except sample PLA2 (1,900 m) that contains two zircons with eU values above 3,000 ppm. These samples do not display important intra-sample age variation and show mean ZHe ages increasing regularly with elevation from 22.0 ± 1.7 to 32.5 ± 3.3 Ma. The two samples PLA3 (1,622 m) and TET5 (1,900 m) from the top of the profile display similar ZHe ages of 36.2 ± 2.9 and 37.3 ± 3.0 Ma, respectively (Table 1 and Figure 3).

4.1.2. Apatite Fission Tracks (AFT)

In the Carança massif, three new AFT ages have been obtained for samples TET4 (1,390 m) and GAL4 (1,221 m) and ST2 (1,217 m; Figure 4). They are respectively of 17.4 ± 1.7, 15.2 ± 1.4, and 17.4 ± 1.7 Ma, with related mean track lengths of 12.84 ± 0.50, 12.81 ± 0.70, and 12.39 ± 0.50 µm. AFT data and mean track lengths are summarized in Table 2 and shown with literature data in Figure 4.

4.2. AERs and Apparent Exhumation Rates

4.2.1. Hanging Wall of the Têt Fault

In the hanging wall of the Têt fault, AERs are presented only for the South Mérens block (Figure 5a). AERs based on AFT and AHe data suggest a three-stage exhumation scenario defined by the lowest BIC (Figure 5a). Samples between 1,400 and 2,400 m provide AFT central ages between 32.3 ± 3.4 and 38.6 ± 2.4 Ma, corresponding to a mean apparent exhumation rate of 0.48 km/Ma. The uncertainty on this exhumation rate is relatively large

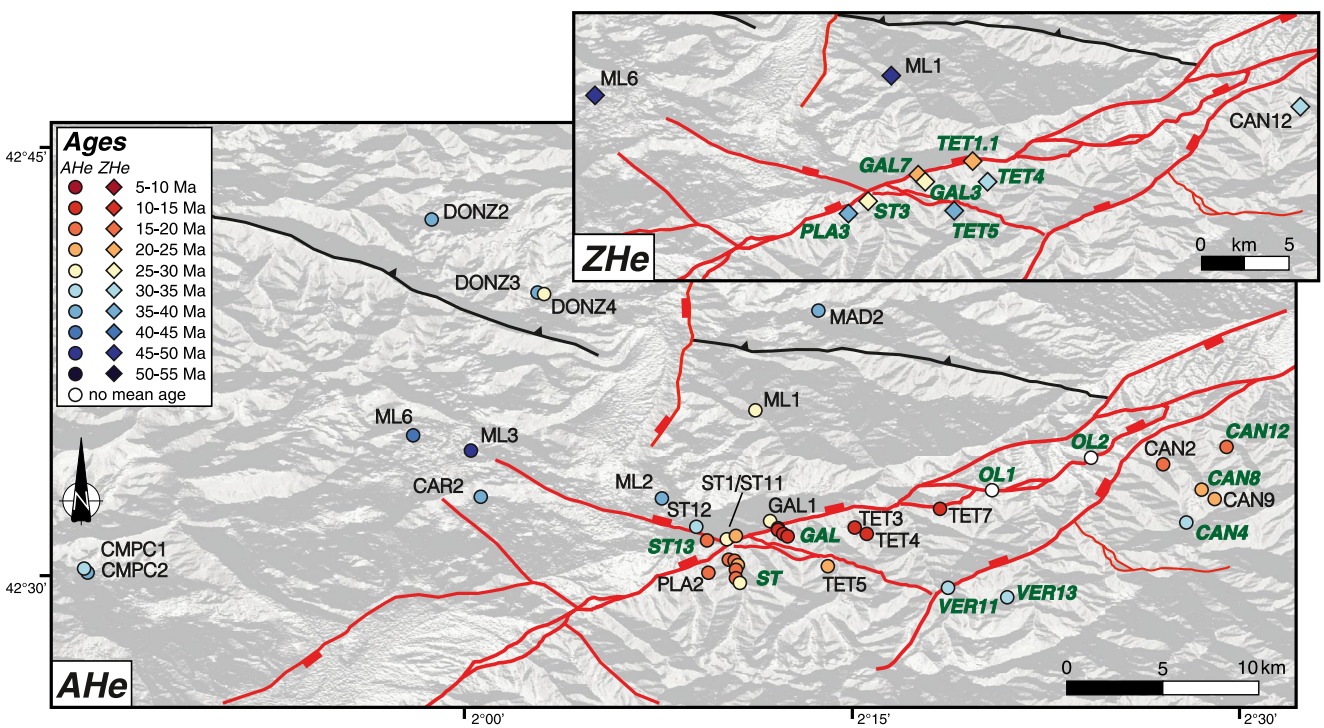

Figure 3. Synthesis of AHe and ZHe ages in the study area. Samples with green labels are new samples from this study, those with black labels are from previous literature studies (Gunnell et al., 2009; Maurel et al., 2008; Milesi, Monié, Münch, et al., 2020; Milesi, Monié, Soliva, et al., 2020; Milesi et al., 2019). Along altitudinal profiles, samples from North to South are: ST profile - ST3, ST4, ST10, ST9, ST8, ST7, ST6; GAL profile—GAL7, GAL6, GAL5, and GAL3. Samples ST6, ST7, ST9, ST10, and GAL5 were dated in this study.

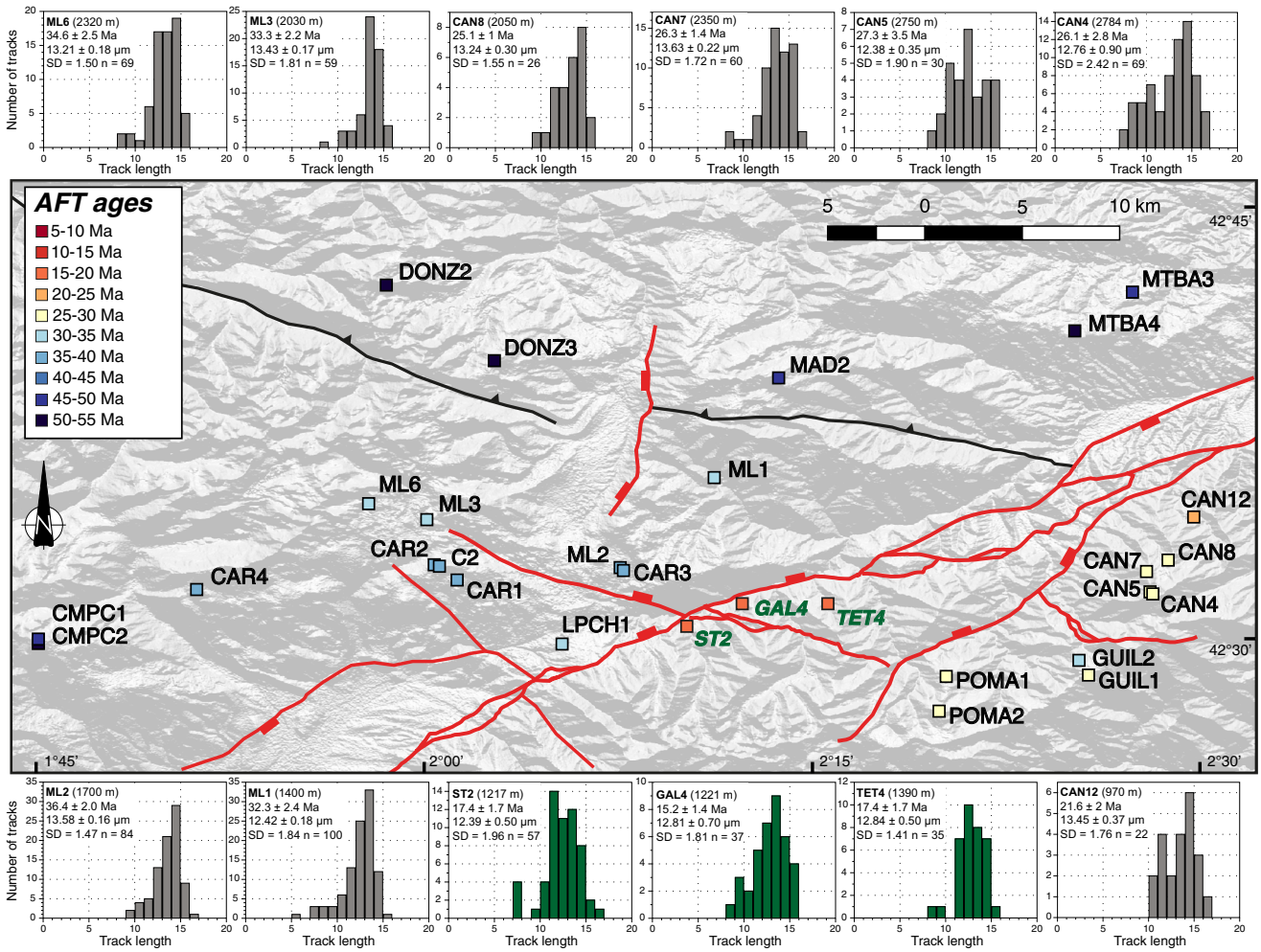

Figure 4. Apatite fission track (AFT) central ages for the study area. Samples ST2, GAL4, and TET4 (in green) are from this study, AFT ages in black have been extracted from Maurel et al. (2008) and Gunnell et al. (2009) (See Table S1 in Supporting Information S1 for details and locations).

(from 0.22 to 1.90 km/Ma) because most samples lie on an apparent vertical straight line. Samples CMPC1 and CMPC2 from the top of the profile (2,900 m), with AFT central ages ~50 Ma, indicate a lower apparent exhumation rate (0.04 km/Ma) that prevailed between ~35 and 50 Ma (Figure 5a, upper graph); although the two ZHe ages in this block suggest potential variability in the exhumation rate during this period. CMPC1 and CMPC2 are the westernmost samples, it may also be possible that they have experienced different exhumations than other samples further East. However, these are the only thermochronological data available above 2,400 m for the South Mérens block, so we cannot assess further this potential difference.

AHe ages from samples above 1,700 m indicate an apparent negative exhumation rate between 35 and 40 Ma. Sample ML3 (2,030 m), which presents an AHe mean age older than its AFT central age has not been considered. This age inversion can find several explanations: an excess helium in the apatite grains (Green et al., 2006), the presence of inclusion inside or rich U-Th grain boundary phases (Murray et al., 2014). Sample ST13 is not presented in Figure 5, its mean AHe age (16.7 ± 1.0 Ma) is younger than that of other samples and cannot be explained by the regional AER trend. The particular structural location of this sample in the footwall of the Fontpédrouse fault, close to the fault corner between Fontpédrouse (NW-SE) and the Têt fault (NE-SW) can explain the specific exhumation history due to the NW-SE fault activity (see Section 2.1). The negative apparent exhumation rate obtained can be due to: (a) the small number of samples (4 in total) above 1,700 m used to precisely define an exhumation rate in this block; (b) a change in AHe kinetics due to the rapid exhumation (e.g., Ault et al., 2019); (c) a major decrease of relief during this period (Braun, 2002; McDannell et al., 2018;

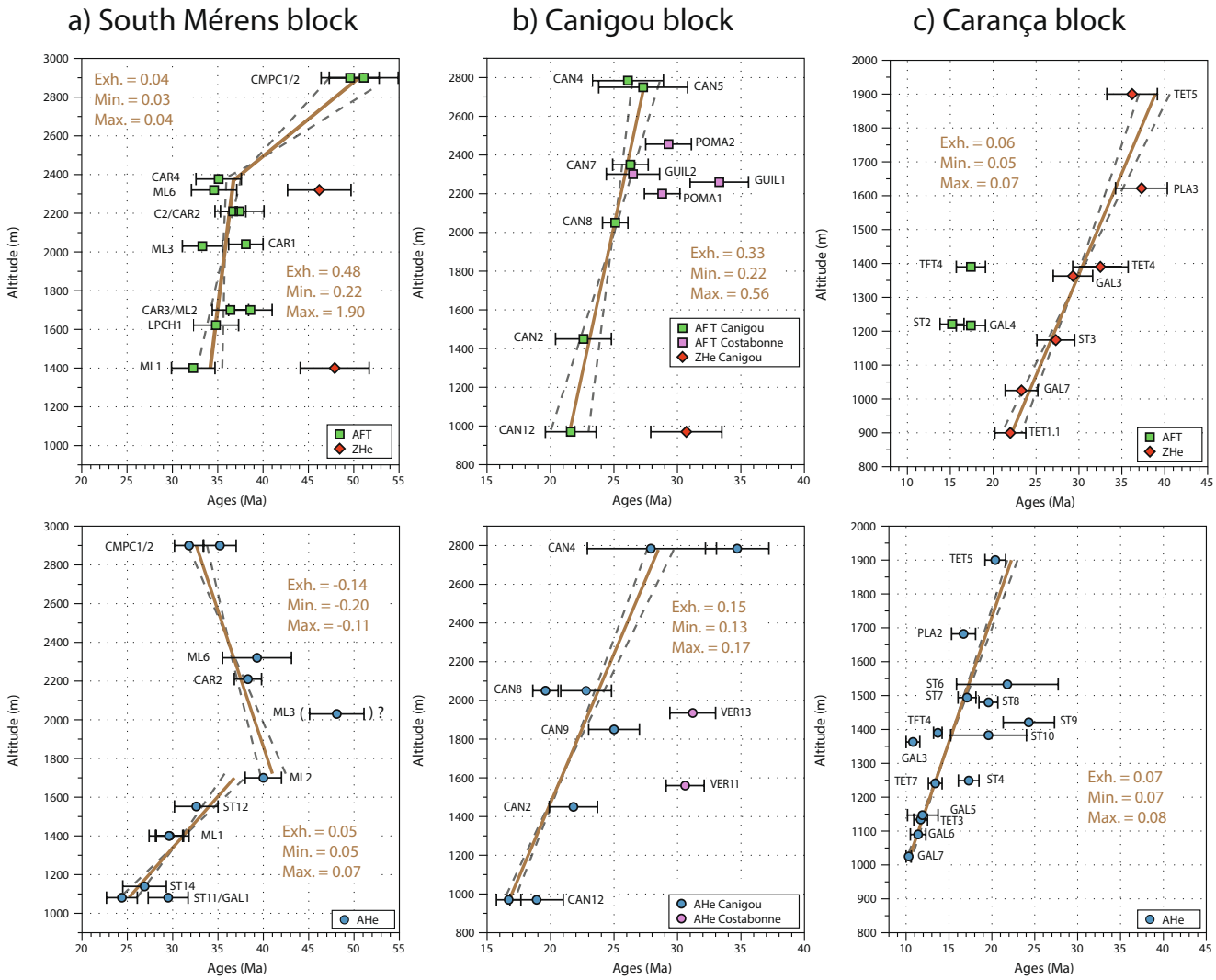

Figure 5. Age-Elevation Relationships (AERs) for AFT and ZHe (first raw) and AHe data (second raw) for (a) the South Mérens block (the AHe mean age of sample ML3 at elevation of 2,050 m, with AHe mean age older than AFT central age has not been considered), (b) the Canigou-Costabonne massif and (c) the Carança massif.

Reiners, 2007). This AER above 1,700 m is strongly influenced by AHe mean ages from CMPC1/2 samples at the top of the profile (Figure 5a, lower graph), and can be explained only by rapid exhumation rates, consistently with the exhumation rates derived from the AFT central ages during this period (Figure 5a, upper graph). Samples between 1,000 and 1,700 m (Figure 5a, lower graph) provide AHe mean ages between 24.2 ± 4.0 and 40.0 ± 2.0 Ma, suggesting an important decrease in the apparent exhumation rate (0.05 km/Ma). For comparison, AFT ages in the North Mérens block support a mean apparent exhumation rate of 0.46 km/Ma between ~52 and 48 Ma, with high uncertainty due to the low number of AFT central ages obtained for this block (see Figure S2 in Supporting Information S1).

4.2.2. Footwall of the Têt Fault

In the footwall of the Têt fault, the Canigou-Costabonne (Figure 5b) and Carança blocks (Figure 5c) are separated by the Py fault and therefore their AERs have been considered individually. In Figure 5b (upper graph), the AER deduced from AFT data in the Canigou sub-block (between 970 and 2,784 m), suggests a single exhumation phase between ca. 22 and 27 Ma, with an apparent exhumation rate of 0.33 km/Ma. AHe mean ages from the same block (Figure 5b, lower graph) are between 16.7 ± 1.8 and 34.7 ± 2.5 Ma, suggesting an apparent exhumation rate of 0.16 km/Ma from the Priabonian to the end of the Burdigalian. South of the Canigou massif, samples

from the Costabonne massif do not show enough elevation difference to provide a reliable exhumation rate from AERs. However, it can be noted that for samples taken at similar elevations in these two massifs, the AFT and AHe ages are 1–10 Ma older in the Costabonne massif than in the Canigou massif (Figure 5b).

In the Carança massif (Figure 5c), both ZHe and AHe data have been used to constrain apparent exhumation rates from AERs. Three AFT central ages cannot be used given the limited elevation distribution (Figure 5c, upper graph). ZHe data obtained on 7 samples show a quasi-ideal AER with an apparent exhumation rate of 0.06 km/Ma between ca. 37 and 22 Ma. AHe data suggest a similar apparent exhumation rate (0.07 km/Ma), between ca. 22 and 10 Ma, with some age variability for samples between 1,250 and 1,550 m on the ST profile, probably due to the proximity of secondary NW-SE faults that locally fragmented the massif in many sub-blocks (Figure 5c, lower graph). We can also note that the AER slope defined between 17 and 15 Ma by the three AFT central ages of the Carança block is in agreement with that derived from AHe mean ages from 20 to 10 Ma (Figure 5c).

4.3. Thermal Evolution

4.3.1. Hanging-Wall of the Têt Fault

The thermal history of the South Mérens block has been derived for all AHe (30) and AFT (12) data from 16 samples used to define AERs (Figure 5a). For this block, the two ZHe ages of samples ML1 and ML6 (Figure 3) have been used as time-temperature constraints for numerical modeling. Another model set-up, including AHe ages of ST13 and ML3 samples and without any ZHe constraint, has been considered and is presented in the Supporting Information (Figure S3 in Supporting Information S1). The output thermal evolution, depicted in Figure 6a, shows that between 50 and 38 Ma, the South Mérens block experienced a cooling rate of around 5°C/Ma, followed by an abrupt acceleration in cooling (~30°C/Ma) between 38 and 35 Ma. Then, since 35 Ma, this block was experiencing slow and continuous cooling (<1°C/Ma). Similar results have been observed in the alternative model (Figure S3 in Supporting Information S1), while AHe ages of ST13 and ML3 samples cannot be correctly reproduced (Figure S3 in Supporting Information S1). With the exception of two AHe ages, all predicted AHe, AFT ages and track lengths are consistent with the observed data implemented for inverse modeling (Figure 6a).

4.3.2. Footwall of the Têt Fault

For the Têt footwall, QTQt thermal modeling was conducted successively on the Canigou and Carança blocks, which are separated by the Py fault. In the Canigou block, data available in the Costabonne sub-block were not considered due to the presence of the Llipodère fault between the Canigou and Costabonne sub-blocks (Figure 1b) and the lack of data under 2,200 m (only two samples with AHe method, VER11 and VER13). An alternative modeling set-up with data from Costabonne sub-block is available in the Supporting Information (Figure S3 in Supporting Information S1). The Canigou thermal modeling (Figure 6b) was designed with all the AHe (12), AFT (6) and track-length data from 7 samples available from the bottom to the top of the massif (thermal modeling output without ZHe constraint is available in Figure S3 in Supporting Information S1). The output thermal history suggests an important cooling event until ca. 33 Ma (onset timing not precisely constrained) at around 30°C/Ma, followed by slow cooling (<1°C/Ma) until ca. 26 Ma. A second cooling phase at ~10°C/Ma can be observed between 26 and 19 Ma, followed by slow cooling until present-day. The thermal history reproduces well AHe, AFT ages and mean track lengths, except the AHe age of sample CAN9 (2,100 m) and mean track lengths measured on samples from the Canigou summit (CAN4 and CAN5). Thermal modeling based on data from the Costabonne sub-block (Figure S3 in Supporting Information S1) also suggests rapid cooling (30°C/Ma) for this block between 32 and 29 Ma, followed by slow cooling (<1°C/Ma); however, this model output should be considered with caution due to the small amount of data (4 AFT and 2 AHe). This rapid cooling would be consistent with an early Oligocene cooling phase, before the Oligo-Miocene phase recorded between 26 and 19 Ma for the Canigou massif (Figure 6b).

The modeled thermal history of the Carança block (Figure 6c) is based on AHe (59), AFT (3) and ZHe (24) data from 20 samples. Output thermal history reveals slow cooling (<1°C/Ma) of the massif between 40 and 25 Ma. The main cooling phase at ~20°C/Ma occurred between 25 and 21 Ma, followed by slow cooling (<1°C/Ma) until 12 Ma. A second cooling pulse, of relatively minor magnitude, can be observed between 12 and 9 Ma with a predicted cooling rate of 10°C/Ma, and is followed by slow cooling (<1°C/Ma) since 9 Ma. Despite the important

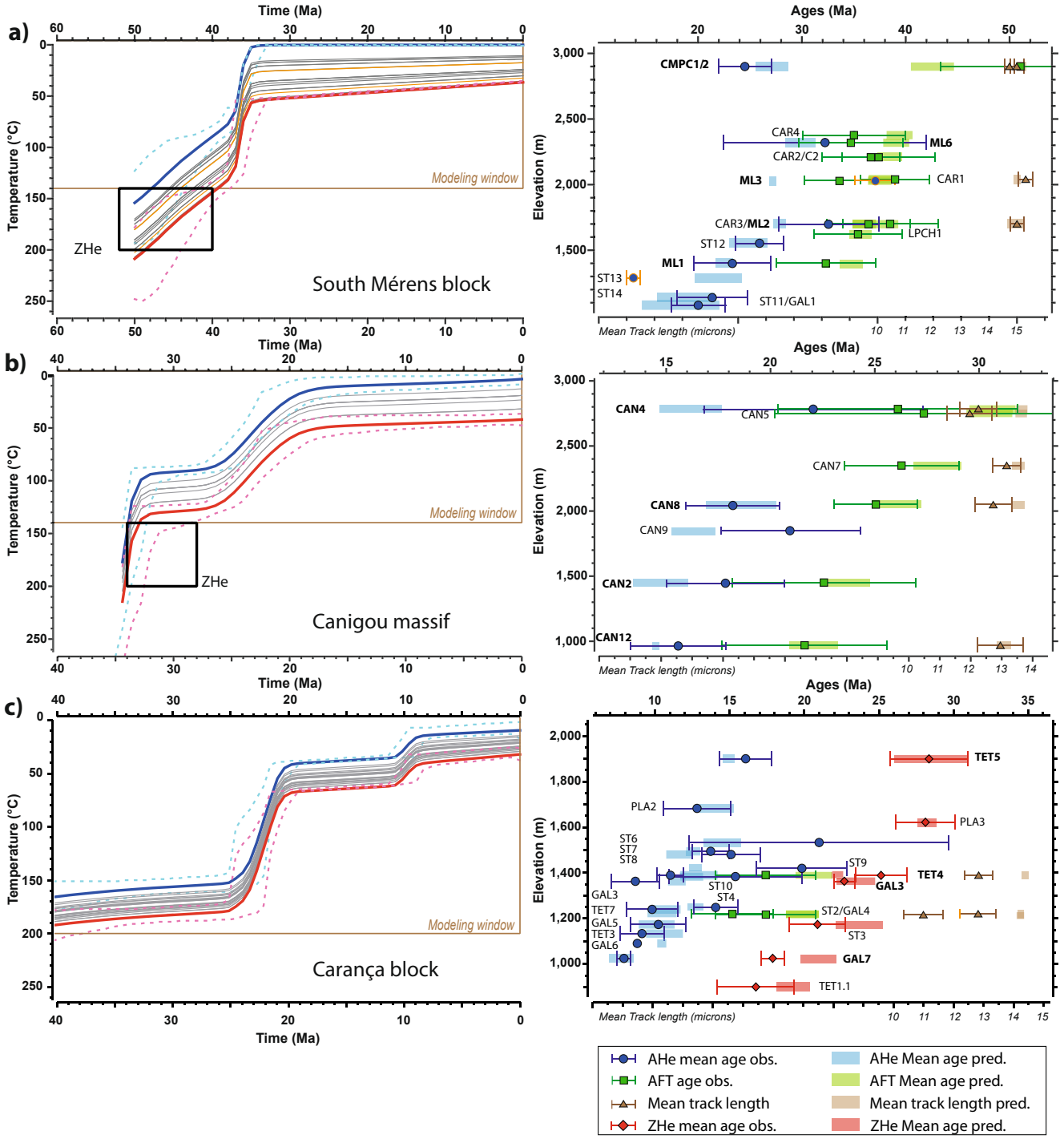

Figure 6. Thermal history of (a) South Mérens block from the hanging wall of the Têt fault, (b) Canigou massif and (c) Carança block from the footwall of the Têt fault. Thermal models were computed using QTQt software (Gallagher, 2012). T-t paths for the uppermost (blue) and the lowermost (red) samples are presented (dashed lines correspond to 95% confidence interval). Black boxes are constraints based on ZHe data from South Mérens block and Canigou massif, ZHe data are modeled for the Carança block. To the right, age-elevation profiles using predicted vs. observed ages for each block are presented as well as observed and predicted track lengths. AHe ages represented with orange error bars in the South Mérens block are not used to construct the thermal evolution model. Sample names for which several thermochronometers were used are indicated in bold. Note that mean predicted/observed data are presented for clarity, but that thermal modeling has been using/predicting single-grain AHe/ZHe data and (U-Th)/He ages (uncorrected for alpha ejection; Farley et al., 1996).

amount of data and an apparent dispersion of AHe ages (see Figure 6c), the modeled thermal history reproduces well the AHe ages (except for samples GAL6, GAL3, ST6, and ST9), AFT ages and ZHe ages (except for sample GAL7). However, we can note that the predicted mean track lengths are not well reproduced and are generally longer than the observed ones (Figure 6c).

5. Discussion

5.1. The Têt Fault Hanging Wall: Contractional Stage

In the hanging wall of the Têt fault, North and South Mérens blocks were distinguished in the present study. In the North Mérens block, AHe mean ages are between 30 and 40 Ma (Figure 3), while AFT central ages are between 45 and 54 Ma (Figure 4 and Figure S3 in Supporting Information S1). These ages are older than those obtained at similar elevations in the South Mérens block. This difference in low-T thermochronological data suggests an early exhumation of the North Mérens block during the Early Eocene, which is in agreement with McCaig and Miller (1986), who proposed on the basis of of $^{40}Ar/^{39}Ar$ mica dating that the Mérens fault was reactivated southward around 50–60 Ma. The scarcity of data in the North Mérens block has not allowed to perform thermal modeling.

The thermal history of the South Mérens block (Figure 6a), obtained using AHe and AFT data, highlights a first stage of cooling between 50 and 38 Ma (>5°C/Ma), that is coeval with a period of maximum shortening in the Eastern Pyrenees that has been evidenced in the Agly-Salvezines massifs to the North of our study area (Ternois et al., 2019). This cooling stage became more rapid between 38 and 35 Ma (~30°C/Ma, Figure 6a). The fast exhumation rate that prevailed during this last cooling stage (0.45 km/Ma from AER, Figure 5a) can be associated with the activity of the Cadi-Canigou thrust fault that emerges further South (Ternois et al., 2019). This thrust is one of the major fault accommodating the convergence between the Iberian and European plates during the Eocene (also see Bosch et al., 2016; Cruset el al., 2020; Fitzgerald et al., 1999; Labaume et al., 2016; Mouthereau et al., 2014; Rushlow et al., 2013; Whitchurch et al., 2011). This interpretation is also consistent with the general propagation and stacking of the nappes from the North to the South in the Pyrenees (Cruset et al., 2020; Fillon & van der Beek, 2012; Jolivet et al., 2007).

At around 35 Ma, our thermal model output suggests that nearly all the samples collected from 1,100 to 2,900 m were above their respective PAZ and PRZ. After 35 Ma, low cooling rates are consistent with an important decrease in exhumation toward present-day in the Têt-fault hanging wall (Figure 5a). This is in agreement with the recent exhumation model for the Axial Zone proposed by Curry et al. (2021). On the basis of a regional thermochronological data compilation and thermo-kinematic modeling (for details see Curry et al., 2021), this exhumation model suggests that rock uplift rates peak at 30–40 Ma in the Eastern Pyrenees, about 10 Ma earlier than in the western Pyrenees (see also Fillon & van der Beek, 2012 for a similar conclusion).

5.2. The Têt Fault Footwall: Extensional Stage

In the different crustal blocks from the southern Têt fault footwall, we used a large number of ZHe, AFT, and AHe data to constrain output thermal histories that emphasize multiple cooling phases since the end of the Eocene (Figure 7). A first fast cooling (~25°C/Ma), that started at an unconstrained period but ended at ca. 33 Ma, is recorded essentially by samples from the top of the Canigou massif (CAN4 and CAN5). Within these two samples, the differences between modeled and observed mean track lengths (Figure 6b) can be explained by the small amount of measured tracks ($n = 30$ and 69, respectively, see Figure 4). We can note that zircon fission track ages of Maurel et al. (2008) from the top and bottom of the Canigou massif are very similar (30.9 ± 2.5 and 33.8 ± 2.1 Ma respectively, see Table S1 in Supporting Information S1). This suggests an important exhumation step of at least 2,000 m during the Priabonian-Rupelian period, which is not recorded further West in the Carança block by the ZHe data (Figure 5c). Thermochronological data from the Costabonne masssif are also consistent with an early Rupelian cooling phase in the Py fault footwall (Figure S3 in Supporting Information S1). The Py normal fault is a NW dipping master fault between the Canigou and Costabonne massifs (with numerous field evidence of substantial displacement: triangular facets, metric fault core with gouges) that branches out on the Têt fault to the North (Figures 1 and 2).

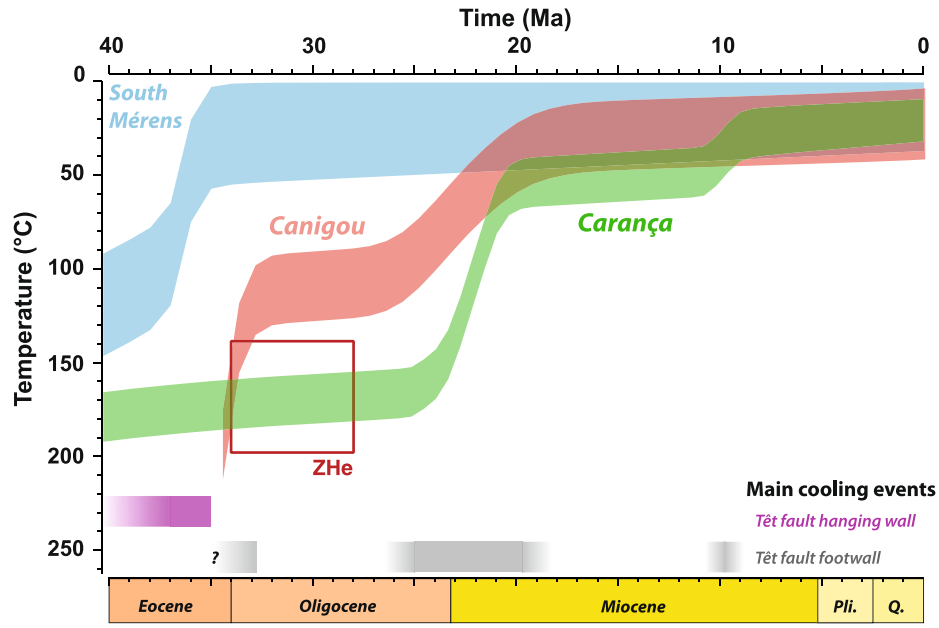

Figure 7. Output thermal histories for the study area: the South Mérens block (blue), the Canigou massif (red, with the associated box for ZHe constraint) and the Carança block (green). Thermal models were computed using QTQt software (Gallagher, 2012). Main cooling events are indicated by purple (hanging wall of the Têt fault) and gray (footwall of the Têt fault) bars.

This important exhumation signal in the Canigou and Costabonne massifs is better explained by normal faulting rather than south-verging thrusting at the regional scale, such as described further South of the study area (e.g., Cruset et al., 2020). We propose that this interpretation of exhumation before 33 Ma is only relevant to the Canigou and Costabonne massifs (Figures 1 and 6) and not to the whole Canigou-Carança range in agreement with Ternois et al. (2019). The Têt and Py faults had probably both accommodated the main exhumation of the Canigou and Costabonne blocks, the normal activity of the Py fault (or both faults) resulting in maintaining the Carança block at depth to the West. Normal activity of the western part of the Têt fault (Carança block) cannot be excluded due to the connection between the Py and the Têt faults (Figure 1). The normal activity of the Py fault thus explains why the low-T thermochronometers used in our study do not record any cooling below PRZ nor PAZ during this period in the Carança block. In a contractional context, the diachronism between the Canigou and Carança blocks would require the presence of a master reverse back-thrust between these two blocks, which is not supported by field observations along the Py fault. Because the South Mérens block was already at shallow crustal level and thus has not recorded any significant cooling/exhumation since 35 Ma, both the Py fault and the southeasternmost segment of the Têt fault were probably active during the Priabonian-Rupelian period to allow for the exhumation of the Canigou-Costabonne massifs only.

The second major cooling event from our output thermal histories occurred between the upper Oligocene and the lower Miocene (i.e., ca. 26–19 Ma), and was recorded by both the Canigou and the Carança massifs (Figure 7). During this period, the Canigou massif experienced relatively fast exhumation (0.33 km/Ma from AER, Figure 5b). This cooling/exhumation signal can be thus associated to normal faulting all along the Têt fault. In the Canigou massif, low-T thermochronology data do not document any major cooling/exhumation since 19 Ma, suggesting that the southeastern segment of the Têt fault remained partly inactive since the Burdigalian. This is in agreement with the sedimentary record in the Conflent basin, showing that the main subsidence, associated with normal activity of the eastern segment of the Têt fault, was concentrated from the Aquitanian to the Early Burdigalian (Calvet et al., 2014). In addition, the AHe mean ages (mostly older than 40 Ma) obtained on gneiss samples from the olistotrome formation in the Conflent basin suggest that the olistolithes collapsed during this upper Oligocene-lower Miocene phase of significant exhumation. Indeed, AHe mean ages from the olistotrome formation are older than for modern bedrock samples at the top of the Canigou profile (AHe mean ages about 30 Ma, Figure 5b). These old ages also show that the olistolithes were not buried enough to reset the AHe signal.

In the Carança block, our AHe data allow to differentiate two sub-blocks separated by the NW-SE Fontpédrouse fault (Figures 1 and 3). AHe mean ages from the eastern sub-block (TET and GAL samples) are younger (10–15 Ma) than for the western sub-block (ST and PLA samples) collected at similar elevations (15–25 Ma, Figure 3). This AHe age difference is obvious for samples between 1,250 and 1,550 m (Figure 5c). In addition, the Fontpédrouse normal fault propagates in the South Mérens block, and it seems likely that the AHe mean age of 16.7 ± 1.0 Ma obtained close to this fault (sample ST13) recorded the fault activity during the Burdigalian (see also alternative thermal modeling in Figure S3 in Supporting Information S1). Note that despite the proximity of a huge gouge zone and evidence for fluid alteration, the Rare Earth Element distribution of this sample remains unaffected by hydrothermalism (see Figure S4 in Supporting Information S1) compared to our previous observations along the Têt fault itself (Milesi, Monié, Münch, et al., 2020). NW-SE trending faults are frequent in this western segment of the Têt fault (see Milesi, 2020; Taillefer et al., 2021) and their activity can account for an important segmentation of the Carança massif with therefore a spatial variability in AHe data due to slightly different cooling histories within the different sub-blocks. In spite of these local perturbations by NW-SE faults in the Carança block, AHe and ZHe data are well reproduced by the QTQt model (Figure 6c), and only mean track lengths show important differences between observed and modeled data, which can be explained by the small amount of tracks measured on the three samples (see Table 2 for details).

A third cooling event has been recorded between 12 and 9 Ma (Serravallian-Tortonian) but only for the Carança block (Figure 7). The lack of record in the Canigou-Costabonne and South Mérens crustal blocks suggests a tectonic activity limited to the southwestern segment of the Têt fault, rather than a general exhumation of the eastern part of the Pyrenees (Calvet et al., 2021; Huyghe et al., 2020). This relatively recent activity can explain the preservation of triangular facet. along the Têt fault (Delmas et al., 2018; Petit & Mouthereau, 2012) and is also consistent with the syntectonic sedimentation of late-Miocene age recorded by the lower unit in the Cerdagne basin (Agustí & Roca, 1987; Pous et al., 1986; Roca, 1996). The opening of the Cerdagne pull-apart sedimentary basins appears essentially controlled by the development of the NW-SE normal faults, facilitated by pre-existing NW-SE segments along the Têt fault (Cabrera et al., 1988).

5.3. Fault System Evolution Model and Geodynamic Implications

In the eastern part of the Pyrenees, North-South shortening has been recorded until ca. 35 Ma by our low-T thermochronological data. This is consistent with the timing for late contractional episode on the North Pyrenean Thrust Front (Grool et al., 2018) and the last main peak of Pyrenean activity (Bartonian-Priabonian) recorded in Provence (Lacombe & Jolivet, 2005). On another side, new U-Pb on calcite studies suggest that shortening in the external units of the Pyrenees proceeded until the middle Miocene (Cruset et al., 2020; Hoareau et al., 2021; Parizot et al., 2021), which could be a consequence of the far-field stress imposed by Africa-Europe convergence (Jolivet, Baudin, et al., 2021; Mouthereau et al., 2021). Based on the sedimentary record, a recent study in the Gulf of Lion margin revealed that the shift between the Pyrenean contractional and extensional tectonics occurred during the late Rupelian (~30 Ma, Séranne et al., 2021), with evidence for a rapid change in the tectonic regime. Although the timing of this shift in tectonic regime is globally consistent (see Section 5.2), our results suggest a slightly earlier onset of normal faulting along the Py and Têt faults, that is, during the Priabonian, and an end of extensional tectonics at ca. 33 Ma (Figure 7). We should also note that previous thermochronological studies proposed a large-scale episode of exhumation recorded in the Eastern Pyrenees between 35 and 30 Ma (Morris et al., 1998) that could be regarded as a consequence of normal faulting, rather than thrusting. This first extensional event preceded a ~7 Ma long period of exhumation quiescence between 33 and 26 Ma (Figure 7), which is synchronous to the development of back-arc extension in the Mediterranean domain (onset at 32–30 Ma, Jolivet & Faccenna, 2000). Thus the first exhumation and coeval extensional tectonic phase does not appear to be related to the rifting phase leading to the opening of the Liguro-Provençal domain, especially with regard to the specific configuration of the Py fault (Figure 8a, i.e., oriented N030°E compared to the N060°E main trend of the Gulf of Lion faults). This event may rather correspond to the West European Rifting from strain geometry and age of exhumation (Angrand & Mouthereau, 2021; Jolivet, Baudin, et al., 2021; Mouthereau et al., 2021; Romagny et al., 2020; Séranne et al., 2021; Ziegler, 1992). The West European Rifting is considered geodynamically independent and can lead or be immediately followed by the Gulf of Lion opening (Jolivet et al., 2015, 2020; Réhault et al., 1987; Séranne, 1999; Vignaroli et al., 2008).

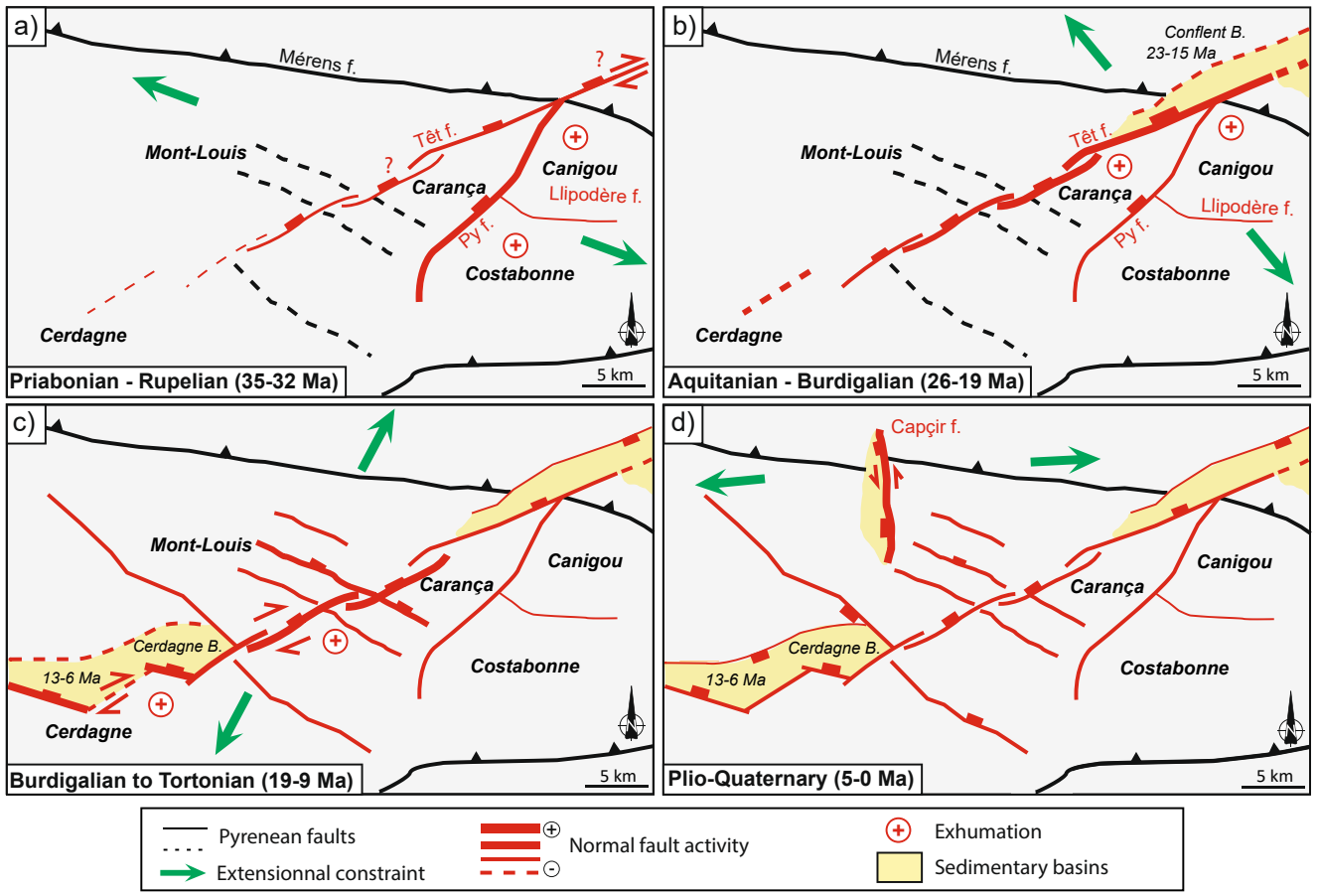

Figure 8. Reconstitution of the extensional tectonic evolution since the Priabonian in the eastern part of the Pyrenees. (a) Priabonian-Rupelian period (35–32 Ma) is marked by the exhumation of the Canigou-Costabonne massif, linked to the Py fault normal motion. A WNW-ESE direction of extension is proposed. (b) Aquitanian-Burdigalian period (26–19 Ma) is characterized by the opening of the Gulf of Lion and normal motion of the Têt fault, more pronounced on the eastern segment of the fault. This observation is in agreement with the early formation of the Conflent basin at 23 Ma. During this period, the Têt fault normal activity is associated to a change toward the North of extensional direction (c) Burdigalian to Tortonian period (19–9 Ma) reveals a propagation further West of the exhumation along the Têt fault with late cooling event recorded for the Carança massif. Local (re-)activation of the NW-SE faults can be involved in AHe dispersion for this block. To the West, the formation of the Cerdagne basin during the Seravallian (13 Ma) is consistent with a spatial migration of the tectonic activity. Normal activity of the NW-SE faults and NE-SW Têt fault is possible under NNE-SSW extension. (d) Plio-Quaternary period (5–0 Ma) is marked by a N-S fault activation (Capçir f.) and E-W direction of extension (Calvet, 1999; Rigo et al., 2015).

A second extensional event has been recorded between the upper Oligocene and Burdigalian for the whole Canigou-Carança range, associated to a main normal faulting phase along the Têt fault (Figures 7 and 8b). This event corresponds to the main cooling event recorded by Maurel et al. (2008), and it appears to be related to the opening of the Gulf of Lion, consistently with sedimentary records on the Catalan margin (Bartrina et al., 1992). In terms of the direction of extension (NW-SE), this event clearly corresponds to the NE-SW trend of the faults observed in the Languedoc, Roussillon, Catalan and Valencia troughs, as well as offshore faults observed at the margin of the Gulf of Lion (e.g., Jolivet, Menant, et al., 2021; Maillard et al., 2020; Mauffret et al., 2001; Romagny et al., 2020; Séranne, 1999). In terms of timing, this second extensional event appears slightly younger than the onset of rifting in Languedoc (late Rupelian, Séranne, 1999), and earlier than the second stage of normal faulting on the Catalan margin (Roca & Desegaulx, 1992), probably reflecting the rift propagation toward the Southwest (Séranne, 1999).

A third extensional event (Figure 8c) has been recorded by AHe data in the Carança and the South Mérens blocks, not in the Canigou-Costabonne block (Figure 3). In the Carança massif, AHe data suggest a change in the direction of extension from NW-SE to NE-SW during the Lower-Miocene times (ca. 18 Ma), with normal-sense mouvement on the NW-SE Fontpédrouse fault. This stage evolved afterward between 12 and 9 Ma on the southwestern segment of the Têt fault, commonly associated to a reactivation stage with moderate normal

displacements between 150 and 500 m (Agustí et al., 2006; Calvet, 1999; Carozza & Baize, 2004; Clauzon et al., 1987, 2015; Delcaillau et al., 2004; Pous et al., 1986; Réhault et al., 1987; Roca & Desegaulx, 1992; Tassone et al., 1994). AHe data along the Têt fault reveal that the exhumation was probably more pronounced along the southwestern segment (>500 m). This stage, that is not recorded by low-T thermochronology data in the Canigou massif (Maurel et al., 2008, this study), marks differential exhumation along the Têt fault, more pronounced at this stage in the southwestern part, consistently with sediment infills of the Cerdagne basin (Agustí et al., 2006; Pous et al., 1986). This late activity on the southwestern segment of the Têt fault confirms the southwestward propagation of the exhumation along the Têt fault (Carozza & Baize, 2004; Carozza & Delcaillau, 1999). The direction of extension is also consistent with Middle-Miocene to Pliocene normal faulting in the Emporda basin and the North-Catalan Ranges that trends globally NW-SE (Lewis et al., 2000; Medialdea et al., 1994; Saula et al., 1994; Taillefer et al., 2021; Tassone et al., 1994). Moreover, the pull-apart opening of the Cerdagne basin, accommodated by normal activity of NW-SE to E-W faults (Agustí et al., 2006; Pous et al., 1986) and right-lateral displacements on NE-SW faults (Cabrera et al., 1988), suggests that the main direction of extension was NNE-SSW, allowing the NE-SW Têt fault to be reactivated in right-lateral strike slip mouvement (Figure 8, Cabrera et al., 1988; Carozza & Baize, 2004; Delcaillau et al., 2004; Goula et al., 1999). We should also note that this trend of extension is also compatible with the stress tensors obtained in the Cerdagne area by Cruset et al. (2020). NW-SE faults could therefore have contributed to the uplift of the Cerdagne basin during Middle Miocene (Calvet et al., 2021; Huyghe et al., 2020; Tosal et al., 2021).

This Lower-Miocene change in direction of extension could be related to geodynamic processes implying stress changes at the Mediterranean domain scale. Romagny et al. (2020) proposed a global change in the main direction of slab retreat at about 20 Ma, with a change in the direction of retreat from NNW-SSE to mostly E-W toward the Appenines. Although at far distance from our study area and not clearly kinematically consistent, such process involving mantle flux perturbations may have implied stress changes at far distances in the Pyrenean lithosphere. Another potential source of stress perturbation could be the mechanical interaction and linkage (e.g., Crider & Pollard, 1998; Kattenhorn et al., 2000) between the Cevennes and the Catalan lithospheric normal faults, through a very large-scale relay zone located in the Eastern Pyrenees. Such large-scale mechanical interaction could have favored stress changes and strain distribution along multiple faults in this eastern part of the Pyrenees. Linkage had to develop with new NW-SE relay faults after the growth of the two NE-SW Cevennes and Penedes master faults in the Oligocene—Lower Miocene (e.g., Séranne et al., 1999), consistently with the timing and direction of the Upper Miocene NW-SE faults observed in the study area. Also note that both master fault segmentation at the place of the pre-existing Pyrenees and the timing of linkage are consistent with the margin development in the Roussillon and its specific orientation (NNW-SSE) in the Gulf of Lion (Mauffret et al., 2001). Finally, another hypothesis to consider is the presence of a new extensional phase due to a not well known geodynamic process in the area (e.g., stresses due to wedge collapse, erosion, or new mantle dynamic, etc.) in a larger domain since a similar cooling event has been recorded in the western Axial Zone (Fillon et al., 2021).

During the Plio-quaternary period (Figure 8d), seismic data inversion highlight a global N-S contraction in the area, while we can note E-W extension in the Cerdagne basin (Rigo et al., 2015). This E-W extension can be responsible for the Capçir N-S normal faulting (Baize et al., 2002; Calvet, 1999), kinematically consistent with a recent return to N-S Pyrenean contraction in the study area.

6. Conclusions

Low-temperature thermochronology and inverse thermal modeling reveal successive cooling periods associated to the differential exhumation of crustal blocks along the southern Têt fault. In the hanging wall of the Têt fault, low-T thermochronological data indicate a significant exhumation/cooling period (~30°C/Ma) between 38 and 35 Ma, followed by an important decrease in exhumation/cooling (<1°C/Ma). This slowdown is interpreted as the result of the last Pyrenean contractional stage during the Priabonian. In the Têt fault footwall, we propose that an early exhumation stage of the Canigou-Costabonne block is recorded until 33 Ma (~30°C/Ma) but not in the Carança block (further West), in association to the normal activity of both the Têt and Py faults. These results suggest a rapid switch between contractional and extensional regime in the Eastern Pyrénées during the Priabonian. A second major cooling event (~20°C/Ma) between the Upper Oligocene and Lower Miocene (26–19 Ma) is recorded both in the Canigou and Carança massifs, associated to the major period of activity of the Têt fault linked to the opening of the Gulf of Lion. During the upper Miocene, low-T thermochronological data from solely

the Carança massif suggest a third cooling event (~10°C/Ma) during the Serravallian-Tortonian (12–9 Ma) and its segmentation in different sub-blocks separated by NW-SE faults. Our results reveal a progressive propagation of the deformation toward the Southwest along the Têt fault, and also account for major changes in the direction of extension in the Eastern Pyrenees since the Priabonian.

Conflict of Interest

The authors declare no conflicts of interest relevant to this study.

Data Availability Statement

All the data used in this study can be obtained in the figures, references, and Supporting Information. The data are deposited in Geochron database (http://www.geochron.org/dataset/html/geochron_dataset_2022_02_02_09p5s).

Acknowledgments
Thanks for technical support go to Olivier Bruguier, Lucie Koeller and Léa Causse for ICP-MS analyses, and Cyprien Astoury for apatite and zircon separation. Thanks to V. Combaudon and G. de Montbrun for help during Canigou sampling and apatite preparation for dating and Frédéric Mouthereau and Riccardo Asti for their positive remarks and improvements. P.G.V. acknowledges funding support from the Swiss National Science Foundation SNSF (Grant PP00P2_170559) and the French ANR-PIA program (ANR-18-MPGA-0006). This research received funding from the program TelluS of the Institut National des Sciences de l'Univers, CNRS. This research has been supported by the THERMOFAULT, a project supported by the Region Occitanie (France) involving TLS Geothermics (main sponsor), Géosciences Montpellier, and the TelluS Program of CNRS/INSU.

References

Agustí, J., Oms, O., Furió, M., Pérez-Vila, M.-J., & Roca, E. (2006). The Messinian terrestrial record in the Pyrenees: The case of Can Vilella (Cerdanya basin). *Palaeogeography, Palaeoclimatology, Palaeoecology*, *238*(1–4), 179–189. https://doi.org/10.1016/j.palaeo.2006.03.024

Agustí, J., & Roca, E. (1987). Síntesis biostratigráfica de la fosa de la Cerdanya (Pirineos orientales). *Estudios Geológicos*, *43*(5–6), 521–529.

Angrand, P., & Mouthereau, F. (2021). Evolution of the Alpine orogenic belts in the western Mediterranean region as resolved by the kinematics of the Europe-Africa diffuse plate boundary. *BSGF—Earth Sciences Bulletin*, *192*, 42. https://doi.org/10.1051/bsgf/2021031

Armstrong, P. A., Ehlers, T. A., Chapman, D. S., Farley, K. A., & Kamp, P. J. J. (2003). Exhumation of the central Wasatch Mountains, Utah: 1. Patterns and timing of exhumation deduced from low-temperature thermochronology data. *Journal of Geophysical Research: Solid Earth*, *108*(B3). https://doi.org/10.1029/2001JB001708

Ault, A. K., Gautheron, C., & King, G. E. (2019). Innovations in (U-Th)/He, fission track, and trapped charge thermochronometry with applications to earthquakes, weathering, surface-mantle connections, and the growth and decay of mountains. *Tectonics*, *38*(11), 3705–3739. https://doi.org/10.1029/2018TC005312

Autran, A., Calvet, M., & Delmas, M. (2005). *Carte géologique de la France à 1/50,000, feuille mont-louis*. BRGM.

Baize, S., Cushing, M., Lemeille, F., Granier, T., & Grellet, B. (2002). Inventaire des indices de rupture affectant le quaternaire, en relation avec les grandes structures connues, en France métropolitaine et dans les régions limitrophe. *Mémoires de la Société géologique de France*, *175*, 1–142.

Bartrina, M. T., Cabrera, L., Jurado, M. J., Guimerà, J., & Roca, E. (1992). Evolution of the central Catalan margin of the Valencia trough (western Mediterranean). *Tectonophysics*, *203*(1–4), 219–247. https://doi.org/10.1016/0040-1951(92)90225-U

Beaumont, C., Muñoz, J. A., Hamilton, J., & Fullsack, P. (2000). Factors controlling the Alpine evolution of the central Pyrenees inferred from a comparison of observations and geodynamical models. *Journal of Geophysical Research: Solid Earth*, *105*(B4), 8121–8145. https://doi.org/10.1029/1999JB900390

Bosch, G. V., Teixell, A., Jolivet, M., Labaume, P., Stockli, D., Domènech, M., & Monié, P. (2016). Timing of Eocene-Miocene thrust activity in the western Axial Zone and Chaînons Béarnais (west-central Pyrenees) revealed by multi-method thermochronology. *Comptes Rendus Geoscience*, *348*(3–4), 246–256. https://doi.org/10.1016/j.crte.2016.01.001

Bouchez, J. L., & Gleizes, G. (1995). Two-stage deformation of the Mont-Louis-Andorra granite pluton (Variscan Pyrenees) inferred from magnetic susceptibility anisotropy. *Journal of the Geological Society*, *152*(4), 669–679. https://doi.org/10.1144/gsjgs.152.4.0669

Braun, J. (2002). Quantifying the effect of recent relief changes on age-elevation relationships. *Earth and Planetary Science Letters*, *200*(3–4), 331–343. https://doi.org/10.1016/S0012-821X(02)00638-6

Briais, A., Armijo, R., Winter, T., Tapponnier, P., & Herbecq, A. (1990). Morphological evidence for quaternary normal faulting and seismic hazard in the Eastern Pyrenees. *Annales Tectonicae*, *4*, 19–42.

Brichau, S., Ring, U., Ketcham, R. A., Carter, A., Stockli, D., & Brunel, M. (2006). Constraining the long-term evolution of the slip rate for a major extensional fault system in the central Aegean, Greece, using thermochronology. *Earth and Planetary Science Letters*, *241*(1–2), 293–306. https://doi.org/10.1016/j.epsl.2005.09.065

Burbank, D. W., Puigdefàbregas, C., & Munoz, J. A. (1992). *The chronology of the Eocene tectonic and stratigraphie development of the eastern Pyrenean foreland basin, northeast Spain* (Vol. 20). Geological Society of America Bulletin.

Cabrera, L., Roca, E., & Santanach, P. (1988). Basin formation at the end of a strike slip fault: The Cerdanya basin (Eastern Pyrenees). *Journal of the Geological Society*, *145*(2), 261–268. https://doi.org/10.1144/gsjgs.145.2.0261

Calvet, M. (1996). *Morphogenèse d'une montagne méditerranéenne, les pyrénées orientales* (Vol. 1, p. 1170). Paris: University of Paris.

Calvet, M. (1999). Régimes des contraintes et volumes de relief dans l'est des Pyrénées/stress regimes and volumes of reliefs in the Eastern Pyrenees. *Géomorphologie: Relief, Processus, Environnement*, *5*(3), 253–278. https://doi.org/10.3406/morfo.1999.991

Calvet, M., Autran, A., Wiazemsky, M., Laumonier, B., & Guitard, G. (2015). Carte géologique de la France, 1:50,000 scale, sheet Argelès-sur-Mer/Cerbère (1097). In B.Laumonier, M.Calvet, P.Barbey, P.Guennoc, J.Lambert, J. L.Lenoble, & M.Wiazemsky (Eds.), *Handbook* (p. 149). Orléans: BRGM.

Calvet, M., Gunnell, Y., & Delmas, M. (2014). The Têt River Valley: A condensed record of long-term landscape evolution in the Pyrenees. In M., Fort, M.-F., André (Eds.), *Landscapes and landforms of France* (pp. 127–138). Dordrecht: Springer Netherlands. https://doi.org/10.1007/978-94-007-7022-5_13

Calvet, M., Gunnell, Y., & Laumonier, B. (2021). Denudation history and paleogeography of the Pyrenees and their peripheral basins: An 84 Myr geomorphological perspective. *Earth-Science Reviews*, *215*, 103436. https://doi.org/10.1016/j.earscirev.2020.103436

Carmignani, L., & Kligfield, R. (1990). Crustal extension in the northern Apennines: The transition from compression to extension in the Alpi Apuane core complex. *Tectonics*, *9*(6), 1275–1303. https://doi.org/10.1029/TC009i006p01275

Carozza, J.-M., & Baize, S. (2004). L'escarpement de faille de la Têt est-il le résultat de la tectonique active Plio-Pléistocène ou d'une exhumation Pléistocène. *Comptes Rendus Geoscience*, *336*(3), 217–226. https://doi.org/10.1016/j.crte.2003.10.026

Carozza, J.-M., & Delcaillau, B. (1999). L'enregistrement géomorphologique de la tectonique quaternaire par les nappes alluviales: L'exemple du bassin de la têt (roussillon, France). *Comptes Rendus de l'Academie des Sciences—Series IIA: Earth and Planetary Science*, *329*(10), 735–740. https://doi.org/10.1016/s1251-8050(00)88493-1

Cederbom, C., Larson, S. Å., Tullborg, E.-L., & Stiberg, J.-P. (2000). Fission track thermochronology applied to Phanerozoic thermotectonic events in central and southern Sweden. *Tectonophysics*, *316*(1–2), 153–167. https://doi.org/10.1016/S0040-1951(99)00230-9

Charvin, K., Gallagher, K., Hampson, G. L., & Labourdette, R. (2009). A Bayesian approach to inverse modeling of stratigraphy, part 1: Method. *Basin Research*, *21*(1), 5–25. https://doi.org/10.1111/j.1365-2117.2008.00369.x

Chevrot, S., Sylvander, M., Diaz, J., Martin, R., Mouthereau, F., Manatschal, G., et al. (2018). The non-cylindrical crustal architecture of the Pyrenees. *Scientific Reports*, *8*(1). https://doi.org/10.1038/s41598-018-27889-x

Choukroune, P. (1989). The ECORS Pyrenean deep seismic profile reflection data and the overall structure of an orogenic belt. *Tectonics*, *8*(1), 23–39. https://doi.org/10.1029/TC008i001p00023

Clauzon, G. (1990). Restitution de l'évolution géodynamique néogène du bassin du Roussillon et de l'unité adjacente des Corbières d'après les données écostratigraphiques et paléogéographiques. *Paleobiologie Continentale*, *17*, 125e155.

Clauzon, G., Aguilar, J.-P., & Michaux, J. (1987). Le bassin pliocène du Roussillon (Pyrénées orientales, France): Exemple d'évolution géodynamique d'une ria méditerranéenne consécutive à la crise de salinité messinienne. *Comptes rendus de l'Académie des Sciences*, *2*(304), 585e590.

Clauzon, G., Le Strat, P., Duvail, C., Do Couto, D., Suc, J.-P., Molliex, S., et al. (2015). The Roussillon basin (S. France): A case study to distinguish local and regional events between 6 and 3 Ma. *Marine and Petroleum Geology*, *66*, 18–40. https://doi.org/10.1016/j.marpetgeo.2015.03.012

Cochelin, B., Chardon, D., Denèle, Y., Gumiaux, C., & Le Bayon, B. (2017). Vertical strain partitioning in hot Variscan crust: Syn-convergence escape of the Pyrenees in the Iberian-Armorican syntax. *Bulletin de la Societe Geologique de France*, *188*(6), 39. https://doi.org/10.1051/bsgf/2017206

Colgan, J. P., Dumitru, T. A., Reiners, P. W., Wooden, J. L., & Miller, E. L. (2006). Cenozoic tectonic evolution of the Basin and Range Province in northwestern Nevada. *American Journal of Science*, *306*(8), 616–654. https://doi.org/10.2475/08.2006.02

Colgan, J. P., Shuster, D. L., & Reiners, P. W. (2008). Two-phase Neogene extension in the northwestern Basin and Range recorded in a single thermochronology sample. *Geology*, *36*(8), 631. https://doi.org/10.1130/G24897A.1

Coutand, I., Walsh, M., Louis, B., Chanier, F., Ferrière, J., & Reynaud, J.-Y. (2014). Neogene upper-crustal cooling of the Olympus range (northern Aegean): Major role of Hellenic back-arc extension over propagation of the North Anatolia fault zone. *Terra Nova*, *26*(4), 287–297. https://doi.org/10.1111/ter.12099

Crider, J. G., & Pollard, D. D. (1998). Fault linkage: Three-dimensional mechanical interaction between echelon normal faults. *Journal of Geophysical Research: Solid Earth*, *103*(B10), 24373–24391. https://doi.org/10.1029/98JB01353

Cruset, D., Vergés, J., Albert, R., Gerdes, A., Benedicto, A., Cantarero, I., & Travé, A. (2020). Quantifying deformation processes in the SE Pyrenees using U-Pb dating of fracture-filling calcites. *Journal of the Geological Society*, *177*(6), 1186–1196. https://doi.org/10.1144/jgs2020-014

Curry, M. A. E., Barnes, J. B., & Colgan, J. P. (2016). Testing fault growth models with low-temperature thermochronology in the northwest Basin and Range, USA. *Tectonics*, *35*(10), 2467–2492. https://doi.org/10.1002/2016TC004211

Curry, M. E., van der Beek, P., Huismans, R. S., Wolf, S. G., Fillon, C., & Muñoz, J.-A. (2021). Spatio-temporal patterns of Pyrenean exhumation revealed by inverse thermo-kinematic modeling of a large thermochronologic data set. *Geology*, *49*(6), 738–742. https://doi.org/10.1130/G48687.1

Curry, M. E., van der Beek, P., Huismans, R. S., Wolf, S. G., & Muñoz, J.-A. (2019). Evolving paleotopography and lithospheric flexure of the Pyrenean orogen from 3-D flexural modeling and basin analysis. *Earth and Planetary Science Letters*, *515*, 26–37. https://doi.org/10.1016/j.epsl.2019.03.009

Danišík, M., Štěpančíková, P., & Evans, N. J. (2012). Constraining long-term denudation and faulting history in intraplate regions by multisystem thermochronology: An example of the Sudetic Marginal Fault (Bohemian Massif, central Europe). *Tectonics*, *31*(2). https://doi.org/10.1029/2011TC003012

Deeken, A., Sobel, E. R., Coutand, I., Haschke, M., Riller, U., & Strecker, M. R. (2006). Development of the southern eastern Cordillera, NW Argentina, constrained by apatite fission track thermochronology: From early Cretaceous extension to middle Miocene shortening. *Tectonics*, *25*(6). https://doi.org/10.1029/2005TC001894

Delcaillau, B., Carozza, J.-M., & Font, M. (2004). The northern segment of the Têt fault (Pyrenees-Orientales): Neogene evolution and geomorphic implications. *Bulletin de la Societe Geologique de France*, *175*(3), 257–272. https://doi.org/10.2113/175.3.257

Delmas, M., Calvet, M., Gunnell, Y., Voinchet, P., Manel, C., Braucher, R., et al. (2018). Terrestrial 10Be and electron spin resonance dating of fluvial terraces quantifies quaternary tectonic uplift gradients in the Eastern Pyrenees. *Quaternary Science Reviews*, *193*, 188–211. https://doi.org/10.1016/j.quascirev.2018.06.001

Diaz, J., Vergés, J., Chevrot, S., Antonio-Vigil, A., Ruiz, M., Sylvander, M., & Gallart, J. (2018). Mapping the crustal structure beneath the Eastern Pyrenees. *Tectonophysics*, *744*, 296–309. https://doi.org/10.1016/j.tecto.2018.07.011

Ehlers, T. A., & Farley, K. A. (2003). Apatite (U-Th)/He thermochronometry: Methods and applications to problems in tectonic and surface processes. *Earth and Planetary Science Letters*, *206*(1–2), 1–14. https://doi.org/10.1016/S0012-821X(02)01069-5

Farley, K. A. (2002). (U-Th)/He dating: Techniques, calibrations, and applications. *Reviews in Mineralogy and Geochemistry*, *47*(1), 819–844. https://doi.org/10.2138/rmg.2002.47.18

Farley, K. A., Wolf, R. A., & Silver, L. T. (1996). The effects of long alpha-stopping distances on (U-Th)/He ages. *Geochimica et Cosmochimica Acta*, *60*, 4223–4229. https://doi.org/10.1016/S0016-7037(96)00193-7

Fillon, C., Mouthereau, F., Calassou, S., Pik, R., Bellahsen, N., Gautheron, C., et al. (2021). Post-orogenic exhumation in the western Pyrenees: Evidence for extension driven by pre-orogenic inheritance. *Journal of the Geological Society*, *178*(2). https://doi.org/10.1144/jgs2020-079

Fillon, C., & van der Beek, P. (2012). Post-orogenic evolution of the southern Pyrenees: Constraints from inverse thermo-kinematic modeling of low-temperature thermochronology data. *Basin Research*, *24*(4), 418–436. https://doi.org/10.1111/j.1365-2117.2011.00533.x

Fitzgerald, P. G., & Malusà, M. G. (2019). Concept of the exhumed partial annealing (retention) zone and age-elevation profiles in thermochronology. In M. G.Malusà, & P. G.Fitzgerald (Eds.), *Fission track thermochronology and its application to geology* (pp. 165–189). Cham: Springer International Publishing. https://doi.org/10.1007/978-3-319-89421-8_9

Fitzgerald, P. G., Muñoz, J. A., Coney, P. J., & Baldwin, S. L. (1999). Asymmetric exhumation across the Pyrenean orogen: Implications for the tectonic evolution of a collisional orogen. *Earth and Planetary Science Letters*, *173*(3), 157–170. https://doi.org/10.1016/S0012-821X(99)00225-3

Fitzgerald, P. G., Sorkhabi, R. B., Redfield, T. F., & Stump, E. (1995). Uplift and denudation of the central Alaska range: A case study in the use of apatite fission track thermochronology to determine absolute uplift parameters. *Journal of Geophysical Research: Solid Earth*, *100*(B10), 20175–20191. https://doi.org/10.1029/95JB02150

Foster, D. A., & John, B. E. (1999). Quantifying tectonic exhumation in an extensional orogen with thermochronology: Examples from the southern Basin and Range Province. *Geological Society, London, Special Publications*, *154*(1), 343–364. https://doi.org/10.1144/GSL.SP.1999.154.01.16

Gallagher, K. (2012). Transdimensional inverse thermal history modeling for quantitative thermochronology. *Journal of Geophysical Research: Solid Earth*, *117*(B2). https://doi.org/10.1029/2011JB008825

Gallagher, K., Charvin, K., Nielsen, S., Sambridge, M., & Stephenson, J. (2009). Markov chain Monte Carlo (MCMC) sampling methods to determine optimal models, model resolution, and model choice for Earth Science problems. *Marine and Petroleum Geology*, *26*(4), 525–535. https://doi.org/10.1016/j.marpetgeo.2009.01.003

Gautheron, C., Pinna-Jamme, R., Derycke, A., Ahadi, F., Sanchez, C., Haurine, F., et al. (2021). Analytical protocols and performance for apatite and zircon (U-Th)/He analysis on quadrupole and magnetic sector mass spectrometer systems between 2007 and 2020. *Geochronology*, *3*(1), 351–370. https://doi.org/10.5194/gchron-3-351-2021

Gautheron, C., & Tassan-Got, L. (2010). A Monte Carlo approach to diffusion applied to noble gas/helium thermochronology. *Chemical Geology*, *273*(3–4), 212–224. https://doi.org/10.1016/j.chemgeo.2010.02.023

Gautheron, C., Tassan-Got, L., Barbarand, J., & Pagel, M. (2009). Effect of alpha-damage annealing on apatite (U-Th)/He thermochronology. *Chemical Geology*, *266*(3–4), 157–170. https://doi.org/10.1016/j.chemgeo.2009.06.001

Gibson, M., Sinclair, H. D., Lynn, G. J., & Stuart, F. M. (2007). Late- to post-orogenic exhumation of the central Pyrenees revealed through combined thermochronological data and modeling. *Basin Research*, *19*(3), 323–334. https://doi.org/10.1111/j.1365-2117.2007.00333.x

Glotzbach, C., van der Beek, P. A., & Spiegel, C. (2011). Episodic exhumation and relief growth in the Mont Blanc massif, Western Alps from numerical modeling of thermochronology data. *Earth and Planetary Science Letters*, *304*(3–4), 417–430. https://doi.org/10.1016/j.epsl.2011.02.020

Goula, X., Olivera, C., Fleta, J., Grellet, B., Lindo, R., Rivera, L. A., et al. (1999). Present and recent stress regime in the eastern part of the Pyrenees. *Tectonophysics*, *308*(4), 487–502. https://doi.org/10.1016/S0040-1951(99)00120-1

Green, P. F., Crowhurst, P. V., Duddy, I. R., Japsen, P., & Holford, S. P. (2006). Conflicting (U-Th)/He and fission track ages in apatite: Enhanced He retention, not anomalous annealing behavior. *Earth and Planetary Science Letters*, *250*(3–4), 407–427. https://doi.org/10.1016/j.epsl.2006.08.022

Green, P. F., Duddy, I. R., Laslett, G. M., Hegarty, K. A., Gleadow, A. J. W., & Lovering, J. F. (1989). Thermal annealing of fission tracks in apatite, 4, quantitative modeling techniques and extension to geological timescale. *Journal of Petroleum Geology*, *12*, 111–114. https://doi.org/10.1016/0168-9622(89)90018-3

Grool, A. R., Ford, M., Vergés, J., Huismans, R. S., Christophoul, F., & Dielforder, A. (2018). Insights into the crustal-scale dynamics of a doubly vergent orogen from a quantitative analysis of its forelands: A case study of the Eastern Pyrenees. *Tectonics*, *37*(2), 450–476. https://doi.org/10.1002/2017TC004731

Guenthner, W. R., Reiners, P. W., Ketcham, R. A., Nasdala, L., & Giester, G. (2013). Helium diffusion in natural zircon: Radiation damage, anisotropy, and the interpretation of zircon (U-Th)/He thermochronology. *American Journal of Science*, *313*(3), 145–198. https://doi.org/10.2475/03.2013.01

Guitard, G., Geyssant, J., Laumonier, B., Autran, A., Fonteilles, M., Dalmayrac, B., et al. (1992). *Carte géologique de la France (1/50,000), feuille prades* (p. 1095).

Guitard, G., Laumonier, B., Autran, A., Bandet, Y., & Berger, G. (1998). *Notice explicative, carte géologique France (1/50,000), feuille Prades (1095)*. Orléans: BRGM.

Gunnell, Y., Calvet, M., Brichau, S., Carter, A., Aguilar, J.-P., & Zeyen, H. (2009). Low long-term erosion rates in high-energy mountain belts: Insights from thermo- and biochronology in the Eastern Pyrenees. *Earth and Planetary Science Letters*, *278*(3–4), 208–218. https://doi.org/10.1016/j.epsl.2008.12.004

Hoareau, G., Crognier, N., Lacroix, B., Aubourg, C., Roberts, N. M. W., Niemi, N., et al. (2021). Combination of Δ47 and U-Pb dating in tectonic calcite veins unravel the last pulses related to the Pyrenean Shortening (Spain). *Earth and Planetary Science Letters*, *553*, 116636. https://doi.org/10.1016/j.epsl.2020.116636

Hurford, A. J. (1990). Standardization of fission track dating calibration: Recommendation by the fission track Working Group of the I.U.G.S. Subcommission on geochronology. *Chemical Geology: Isotope Geoscience Section*, *80*(2), 171–178. https://doi.org/10.1016/0168-9622(90)90025-8

Huyghe, D., Mouthereau, F., Ségalen, L., & Furió, M. (2020). Long-term dynamic topographic support during post-orogenic crustal thinning revealed by stable isotope (δ^{18}O) paleo-altimetry in Eastern Pyrenees. *Scientific Reports*, *10*(1), 2267. https://doi.org/10.1038/s41598-020-58903-w

Jolivet, L., Baudin, T., Calassou, S., Chevrot, S., Ford, M., Issautier, B., et al. (2021). Geodynamic evolution of a wide plate boundary in the western Mediterranean, near-field vs. far-field interactions. *BSGF—Earth Sciences Bulletin*, *192*, 48. https://doi.org/10.1051/bsgf/2021043

Jolivet, L., & Faccenna, C. (2000). Mediterranean extension and the Africa-Eurasia collision. *Tectonics*, *19*(6), 1095–1106. https://doi.org/10.1029/2000TC900018

Jolivet, L., Gorini, C., Smit, J., & Leroy, S. (2015). Continental breakup and the dynamics of rifting in back-arc basins: The Gulf of Lion margin. *Tectonics*, *34*(4), 662–679. https://doi.org/10.1002/2014TC003570

Jolivet, L., Menant, A., Roche, V., Le Pourhiet, L., Maillard, A., Augier, R., et al. (2021). Transfer zones in Mediterranean back-arc regions and tear faults. *BSGF—Earth Sciences Bulletin*, *192*, 11. https://doi.org/10.1051/bsgf/2021006

Jolivet, L., Romagny, A., Gorini, C., Maillard, A., Thinon, I., Couëffé, R., et al. (2020). Fast dismantling of a mountain belt by mantle flow: Late-orogenic evolution of Pyrenees and Liguro-Provençal rifting. *Tectonophysics*, *776*, 228312. https://doi.org/10.1016/j.tecto.2019.228312

Jolivet, M., Labaume, P., Monié, P., Brunel, M., Arnaud, N., & Campani, M. (2007). Thermochronology constraints for the propagation sequence of the South Pyrenean basement thrust system (France-Spain). *Tectonics*, *26*(5). https://doi.org/10.1029/2006TC002080

Jones, C. H., & Wesnousky, S. G. (1992). Variations in strength and slip rate along the San Andreas fault system. *Science*, *256*(5053), 83–86. https://doi.org/10.1126/science.256.5053.83

Kattenhorn, S. A., Aydin, A., & Pollard, D. D. (2000). Joints at high angles to normal fault strike: An explanation using 3-D numerical models of fault-perturbed stress fields. *Journal of Structural Geology*, *22*(1), 1–23. https://doi.org/10.1016/S0191-8141(99)00130-3

Ketcham, R. A., Carter, A., Donelick, R. A., Barbarand, J., & Hurford, A. J. (2007). Improved modeling of fission track annealing in apatite. *American Mineralogist*, *92*(5–6), 799–810. https://doi.org/10.2138/am.2007.2281

Ketcham, R. A., Donelick, R. A., & Carlson, W. D. (1999). Variability of apatite fission track annealing kinetics: III. Extrapolation to geological time scales. *American Mineralogist*, *84*(9), 1235–1255. https://doi.org/10.2138/am-1999-0903

Ketcham, R. A., Gautheron, C., & Tassan-Got, L. (2011). Accounting for long alpha-particle stopping distances in (U-Th-Sm)/He geochronology: Refinement of the baseline case. *Geochimica et Cosmochimica Acta*, *75*, 7779–7791. https://doi.org/10.1016/j.gca.2011.10.011

Krugh, W. C. (2008). Low-temperature thermochronologic constraints on fault array evolution and patterns of range-scale denudation. *ETH Zurich*. https://doi.org/10.3929/ETHZ-A-005772437

Labaume, P., Meresse, F., Jolivet, M., Teixell, A., & Lahfid, A. (2016). Tectonothermal history of an exhumed thrust-sheet-top basin: An example from the South Pyrenean thrust belt. *Tectonics*, *35*(5), 1280–1313. https://doi.org/10.1002/2016TC004192

Lacan, P., & Ortuño, M. (2012). Active tectonics of the Pyrenees: A review. *Journal of Iberian Geology*, *38*(1). https://doi.org/10.5209/rev_JIGE.2012.v38.n1.39203

Lacombe, O., & Jolivet, L. (2005). Structural and kinematic relationships between Corsica and the Pyrenees-Provence domain at the time of the Pyrenean orogeny. *Tectonics*, *24*(1). https://doi.org/10.1029/2004TC001673

Laumonier, B., Calvet, M., Delmas, M., Barbey, P., Lenoble, J., & Autran, A. (2017). Notice explicative Carte géologique de la France `a 1/50,000, feuille Mont-Louis (1094). In (p. 139). Orléans: BRGM.

Laumonier, B., Calvet, M., Le Bayon, B., Barbey, P., & Lenoble, J.-L. (2015). Avec la collaboration de Cocherie A., Melleton J.—Notice explicative, Carte géologique de la France à 1/50 000, feuille Prats-de-Mollo-la-Preste (1099). In: *Orléans: BRGM*, (p.189).

Lewis, C. J., Vergés, J., & Marzo, M. (2000). High mountains in a zone of extended crust: Insights into the Neogene-Quaternary topographic development of northeastern Iberia. *Tectonics*, *19*(1), 86–102. https://doi.org/10.1029/1999TC900056

Maillard, A., Jolivet, L., Lofi, J., Thinon, I., Couëffé, R., Canva, A., & Dofal, A. (2020). Transfer zones and associated volcanic province in the eastern Valencia basin: Evidence for a hot rifted margin?*Marine and Petroleum Geology*, 104419. https://doi.org/10.1016/j.marpetgeo.2020.104419

Malusà, M. G., Polino, R., & Zattin, M. (2009). Strain partitioning in the axial NW Alps since the Oligocene. *Tectonics*, *28*(3). https://doi.org/10.1029/2008TC002370

Malusà, M. G., Polino, R., Zattin, M., Bigazzi, G., Martin, S., & Piana, F. (2005). Miocene to Present differential exhumation in the Western Alps: Insights from fission track thermochronology. *Tectonics*, *24*(3). https://doi.org/10.1029/2004TC001782

Martín-González, F., Barbero, L., Capote, R., Heredia, N., & Gallastegui, G. (2012). Interaction of two successive Alpine deformation fronts: Constraints from low-temperature thermochronology and structural mapping (NW Iberian Peninsula). *International Journal of Earth Sciences*, *101*(5), 1331–1342. https://doi.org/10.1007/s00531-011-0712-9

Mauffret, A., Durand de Grossouvre, B., Tadeu Dos Reis, A., Gorini, C., & Nercessian, A. (2001). Structural geometry in the Eastern Pyrenees and western Gulf of Lion (western Mediterranean). *Journal of Structural Geology*, *23*(11), 1701–1726. https://doi.org/10.1016/S0191-8141(01)00025-6

Maurel, O., Brunel, M., & Monié, P. (2002). Exhumation cénozoïque des massifs du Canigou et de Mont-Louis (Pyrénées orientales, France). *Comptes Rendus Geoscience*, *334*(12), 941–948. https://doi.org/10.1016/S1631-0713(02)01834-5

Maurel, O., Moniè, P., Pik, R., Arnaud, N., Brunel, M., & Jolivet, M. (2008). The Meso-Cenozoic thermo-tectonic evolution of the Eastern Pyrenees: An $^{40}Ar/^{39}Ar$ fission track and (U-Th)/He thermochronological study of the Canigou and Mont-Louis massifs. *International Journal of Earth Sciences*, *97*(3), 565–584. https://doi.org/10.1007/s00531-007-0179-x

McCaig, A. M., & Miller, J. A. (1986). ^{40}Ar-^{39}Ar age of mylonites along the Merens fault, central Pyrenees. *Tectonophysics*, *129*(1–4), 149–172. https://doi.org/10.1016/0040-1951(86)90250-7

McDannell, K. T., Zeitler, P. K., & Idleman, B. D. (2018). Relict topography within the Hangay Mountains in Central Mongolia: Quantifying long-term exhumation and relief change in an old landscape. *Tectonics*, *37*(8), 2531–2558. https://doi.org/10.1029/2017TC004682

McDowell, F. W., McIntosh, W. C., & Farley, K. A. (2005). A precise ^{40}Ar-^{39}Ar reference age for the Durango apatite (U-Th)/He and fission track dating standard. *Chemical Geology*, *214*, 249–263. https://doi.org/10.1016/j.chemgeo.2004.10.002

Medialdea, T., Vázquez, J., & Vegas, R. (1994). Estructura y evolucion geodinamica del extremo noreste del margen continental catalán durante el néogeno. *Acta Geológica Hispánica*, *29*(2–4), 39–53.

Metcalf, J. R., Fitzgerald, P. G., Baldwin, S. L., & Muñoz, J.-A. (2009). Thermochronology of a convergent orogen: Constraints on the timing of thrust faulting and subsequent exhumation of the Maladeta Pluton in the central Pyrenean Axial Zone. *Earth and Planetary Science Letters*, *287*(3–4), 488–503. https://doi.org/10.1016/j.epsl.2009.08.036

Milesi, G. (2020). *Analyse thermochronologique, géochimique et structurale du système hydrothermal de la faille de la Têt (Pyrénées, France), un nouvel outil d'exploration géothermique* (PhD thesis). Université de Montpellier.

Milesi, G., Monié, P., Münch, P., Soliva, R., Taillefer, A., Bruguier, O., et al. (2020). Tracking geothermal anomalies along a crustal fault using (U-Th)/He apatite thermochronology and rare-earth element (REE) analyses: The example of the Têt fault (Pyrenees, France). *Solid Earth*, *11*(5), 1747–1771. https://doi.org/10.5194/se-11-1747-2020

Milesi, G., Monié, P., Soliva, R., Mûnch, P., Taillefer, A., Bellanger, M., et al. (2020). Imaging geothermal anomalies using low-temperature (U-Th)/He thermochronometry: A case study from the active Têt fault hydrothermal system (Eastern Pyrenees, France). In *Proceedings World Geothermal Congress 2020 Reykjavik, Iceland*. 26 April to 2 May 2020.

Milesi, G., Soliva, R., Monié, P., Münch, P., Bellanger, M., Bruguier, O., et al. (2019). Mapping a geothermal anomaly using apatite (U-Th)/He thermochronology in the Têt fault damage zone, Eastern Pyrenees, France. *Terra Nova*, *31*(6), 569–576. https://doi.org/10.1111/ter.12429

Morris, R. G., Sinclair, H. D., & Yelland, A. J. (1998). Exhumation of the Pyrenean orogen: Implications for sediment discharge. *Basin Research*, *10*, 69–86. https://doi.org/10.1046/j.1365-2117.1998.00053.x

Mouthereau, F., Angrand, P., Jourdon, A., Ternois, S., Fillon, C., Calassou, S., et al. (2021). Cenozoic mountain building and topographic evolution in Western Europe: Impact of billions of years of lithosphere evolution and plate kinematics. *BSGF—Earth Sciences Bulletin*, *192*, 56. https://doi.org/10.1051/bsgf/2021040

Mouthereau, F., Filleaudeau, P.-Y., Vacherat, A., Pik, R., Lacombe, O., Fellin, M. G., et al. (2014). Placing limits to shortening evolution in the Pyrenees: Role of margin architecture and implications for the Iberia/Europe convergence: Plate convergence in the Pyrenees. *Tectonics*, *33*(12), 2283–2314. https://doi.org/10.1002/2014TC003663

Muñoz, J. A. (1992). Evolution of a continental collision belt: ECORS-Pyrenees crustal balanced cross-section. In K. R.,McClay (Ed.), *Thrust tectonics* (pp. 235–246). Dordrecht: Springer Netherlands. https://doi.org/10.1007/978-94-011-3066-0_21

Murray, K. E., Orme, D. A., & Reiners, P. W. (2014). Effects of U-Th-rich grain boundary phases on apatite helium ages. *Chemical Geology*, *390*, 135–151. https://doi.org/10.1016/j.chemgeo.2014.09.023

Nercessian, A., Mau, A., Gallart, J., & Diaz, J. (2001). Deep reflection seismic images of the crustal thinning in the Eastern Pyrenees and western Gulf of Lion. *Journal of Geodynamics*, *15*. https://doi.org/10.1016/S0264-3707(00)00029-6

Norris, R. J., & Cooper, A. F. (2001). Late Quaternary slip rates and slip partitioning on the Alpine Fault, New Zealand. *Journal of Structural Geology*, *23*(2–3), 507–520. https://doi.org/10.1016/S0191-8141(00)00122-X

Parizot, O., Missenard, Y., Haurine, F., Blaise, T., Barbarand, J., Benedicto, A., & Sarda, P. (2021). When did the Pyrenean shortening end? Insight from U-Pb geochronology of syn-faulting calcite (Corbières area, France). *Terra Nova*, *33*(6), 551–559. https://doi.org/10.1111/ter.12547

Petit, C., & Mouthereau, F. (2012). Steep topographic slope preservation by anisotropic diffusion: An example from the Neogene Têt fault scarp, Eastern Pyrenees. *Geomorphology*, *171–172*, 173–179. https://doi.org/10.1016/j.geomorph.2012.05.016

Pous, J., Julià, R., & Sugrañes, L. S. (1986). Cerdanya basin geometry and its implication on the neocene evolution of the Eastern Pyrenees. *Tectonophysics*, *129*(1–4), 355–365. https://doi.org/10.1016/0040-1951(86)90261-1

Price, J. G., & Henry, C. D. (1984). Stress orientations during Oligocene volcanism in Trans-Pecos Texas: Timing the transition from Laramide compression to Basin and Range tension. *Geology*, *12*(4), 238–241. https://doi.org/10.1130/0091-7613(1984)12<238:SODOVI>2.0.CO;2

Ratschbacher, L., Hacker, B. R., Calvert, A., Webb, L. E., Grimmer, J. C., McWilliams, M. O., et al. (2003). Tectonics of the Qinling (central China): Tectonostratigraphy, geochronology, and deformation history. *Tectonophysics*, *366*(1–2), 1–53. https://doi.org/10.1016/S0040-1951(03)00053-2

Réhault, J., Moussat, E., & Fabbri, A. (1987). Structural evolution of the Tyrrhenian back-arc basin. *Marine Geology*, *74*(1–2), 123–150. https://doi.org/10.1016/0025-3227(87)90010-7

Reiners, P. W. (2007). Thermochronologic approaches to paleotopography. *Reviews in Mineralogy and Geochemistry*, *66*(1), 243–267. https://doi.org/10.2138/rmg.2007.66.10

Reiners, P. W., & Brandon, M. T. (2006). Using thermochronology to understand orogenic erosion. *Annual Review of Earth and Planetary Sciences*, *34*(1), 419–466. https://doi.org/10.1146/annurev.earth.34.031405.125202

Reiners, P. W., & Nicolescu, S. (2006). *Measurement of parent nuclides for (U-Th)/He chronometry by solution sector ICP-MS, ARHDL Rep., 1, Ariz. Radiogenic Helium Dating Lab., Tucson*. Retrieved from https://www.geo.arizona.edu/~reiners/arhdl/U-Th-Sm_measurement_Reiners_042107.pdf

Rigo, A., Vernant, P., Feigl, K. L., Goula, X., Khazaradze, G., Talaya, J., et al. (2015). Present-day deformation of the Pyrenees revealed by GPS surveying and earthquake focal mechanisms until 2011. *Geophysical Journal International*, *201*(2), 947–964. https://doi.org/10.1093/gji/ggv052

Roca, E. (1996). The Neogene Cerdanya and Seu d´Urgell intramontane basins (Eastern Pyrenees). In P.Friend, & C. J.Bario (Eds.), *Tertiary basins of Spain. The stratigraphic record of crustal kinematics* (pp. 114–118). Cambridge: Cambridge University Press. https://doi.org/10.1017/cbo9780511524851.019

Roca, E., & Desegaulx, P. (1992). Analysis of the geological evolution and vertical movements in the Valencia trough area, western mediterranean. *Marine and Petroleum Geology*, *9*(2), 167–176. https://doi.org/10.1016/0264-8172(92)90089-w

Roca, E., & Santanach, P. (1986). Génesis y evolucion de la Fosa de la Cerdanya (Pirineos orientales). *Geogaceta*, *1*, 37–38.

Romagny, A., Jolivet, L., Menant, A., Bessière, E., Maillard, A., Canva, A., et al. (2020). Detailed tectonic reconstructions of the western Mediterranean region for the last 35 Ma, insights on driving mechanisms. *BSGF—Earth Sciences Bulletin*, *191*, 37. https://doi.org/10.1051/bsgf/2020040

Roure, F., Choukroune, P., Berastegui, X., Munoz, J. A., Villien, A., Matheron, P., et al. (1989). ECORS deep seismic data and balanced cross-sections: Geometric constraints on the evolution of the Pyrenees. *Tectonics*, *8*(1), 41–50. https://doi.org/10.1029/TC008i001p00041

Rushlow, C. R., Barnes, J. B., Ehlers, T. A., & Vergés, J. (2013). Exhumation of the southern Pyrenean fold-thrust belt (Spain) from orogenic growth to decay. *Tectonics*, *32*(4), 843–860. https://doi.org/10.1002/tect.20030

Sambridge, M. (1999). Geophysical inversion with a neighborhood algorithm—II. Appraising the ensemble. *Geophysical Journal International*, *138*, 727–746. https://doi.org/10.1046/j.1365-246x.1999.00900.x

Sartégou, A., Bourlès, D. L., Blard, P.-H., Braucher, R., Tibari, B., Zimmermann, L., et al. (2018). Deciphering landscape evolution with karstic networks: A Pyrenean case study. *Quaternary Geochronology*, *43*, 12–29. https://doi.org/10.1016/j.quageo.2017.09.005

Saula, E., Picart, J., Mató, E., Llenas, M., Losantos, M., Berástegui, X., & Agustí, J. (1994). Evolución geodinámica de la fosa del Empordà y las Sierras Transversales. *Acta Geológica Hispánica*, *29*(2–4), 55–75.

Schwarz, G. (1978). Estimating the dimension of a model. *Annals of Statistics*, *6*(2), 461–464. https://doi.org/10.1214/aos/1176344136

Séranne, M. (1999). The Gulf of Lion continental margin (NW Mediterranean) revisited by IBS: An overview. *Geological Society, London, Special Publications*, *156*(1), 15–36. https://doi.org/10.1144/GSL.SP.1999.156.01.03

Séranne, M., Benedicto, A., Labaum, P., Truffert, C., & Pascal, G. (1995). Structural style and evolution of the Gulf of Lion Oligo-Miocene rifting: Role of the Pyrenean orogeny. *Marine and Petroleum Geology*, *12*(8), 809–820. https://doi.org/10.1016/0264-8172(95)98849-Z

Séranne, M., Couëffé, R., Husson, E., Baral, C., & Villard, J. (2021). The transition from Pyrenean shortening to Gulf of Lion rifting in Languedoc (South France)—A tectonic-sedimentation analysis. *BSGF—Earth Sciences Bulletin*, *192*(1), 27. https://doi.org/10.1051/bsgf/2021017

Sibuet, J.-C., Srivastava, S. P., & Spakman, W. (2004). Pyrenean orogeny and plate kinematics. *Journal of Geophysical Research: Solid Earth*, *109*(B8). https://doi.org/10.1029/2003JB002514

Sinclair, H. D., Gibson, M., Naylor, M., & Morris, R. G. (2005). Asymmetric growth of the Pyrenees revealed through measurement and modeling of orogenic fluxes. *American Journal of Science*, *305*(5), 369–406. https://doi.org/10.2475/ajs.305.5.369

Stockli, D. F. (2005). Application of low-temperature thermochronometry to extensional tectonic settings. *Reviews in Mineralogy and Geochemistry*, *58*(1), 411–448. https://doi.org/10.2138/rmg.2005.58.16

Stockli, D. F., Farley, K. A., & Dumitru, T. A. (2000). Calibration of the apatite (U-Th)/He thermochronometer on an exhumed fault block, White Mountains, California. *Geology*, *28*(11), 983–986. https://doi.org/10.1130/0091-7613(2000)028<0983:cotaut>2.3.co;2

Stüwe, K., White, L., & Brown, R. (1994). The influence of eroding topography on steady-state isotherms. Application to fission track analysis. *Earth and Planetary Science Letters*, *124*(1–4), 63–74. https://doi.org/10.1016/0012-821X(94)00068-9

Suc, J.-P., & Fauquette, S. (2012). The use of pollen floras as a tool to estimate paleoaltitude of mountains: The Eastern Pyrenees in the late Neogene, a case study. *Palaeogeography, Palaeoclimatology, Palaeoecology*, *321–322*, 41–54. https://doi.org/10.1016/j.palaeo.2012.01.014

Surpless, B. E., Stockli, D. F., Dumitru, T. A., & Miller, E. L. (2002). Two-phase westward encroachment of Basin and Range extension into the northern Sierra Nevada. *Tectonics*, *21*(1), 21–210. https://doi.org/10.1029/2000TC001257

Taillefer, A., Milesi, G., Soliva, R., Monnier, L., Delorme, P., Guillou-Frottier, L., & Le Goff, E. (2021). Polyphased brittle deformation around a crustal fault: A multi-scale approach based on remote sensing and field data on the mountains surrounding the Têt hydrothermal system (Eastern Pyrénées, France). *Tectonophysics*, *804*, 228710. https://doi.org/10.1016/j.tecto.2020.228710

Taillefer, A., Soliva, R., Guillou-Frottier, L., Le Goff, E., Martin, G., & Séranne, M. (2017). Fault-related controls on upward hydrothermal flow: An integrated geological study of the Têt fault system, Eastern Pyrénées (France). *Geofluids*, *2017*, 1–19. https://doi.org/10.1155/2017/8190109

Tassone, A., Roca, E., Muñoz, J. A., Cabrera, L., & Canals, M. (1994). Evolución del sector septentrional del margen continental catalán durante el Cenozoico. *Acta Geológica Hispánica*, *29*(2–4), 3–37.

Teixell, A., Labaume, P., & Lagabrielle, Y. (2016). The crustal evolution of the west-central Pyrenees revisited: Inferences from a new kinematic scenario. *Comptes Rendus Geoscience*, *348*(3–4), 257–267. https://doi.org/10.1016/j.crte.2015.10.010

Ternois, S., Odlum, M., Ford, M., Pik, R., Stockli, D., Tibari, B., et al. (2019). Thermochronological evidence of early orogenesis, Eastern Pyrenees, France. *Tectonics*, *38*(4), 1308–1336. https://doi.org/10.1029/2018TC005254

Tosal, A., Verduzco, O., & Martín-Closas, C. (2021). CLAMP-based paleoclimatic analysis of the late Miocene (Tortonian) flora from La Cerdanya basin of Catalonia, Spain, and an estimation of the paleoaltitude of the Eastern Pyrenees. *Palaeogeography, Palaeoclimatology, Palaeoecology*, *564*, 110186. https://doi.org/10.1016/j.palaeo.2020.110186

Vacherat, A., Mouthereau, F., Pik, R., Huyghe, D., Paquette, J.-L., Christophoul, F., et al. (2016). Rift-to-collision sediment routing in the Pyrenees: A synthesis from sedimentological, geochronological and kinematic constraints. *Earth-Science Reviews*, *172*, 43–74. https://doi.org/10.1016/j.earscirev.2017.07.004

Vergés, J., Fernandez, M., & Martinez, A. (2002). The Pyrenean orogen: Pre-, syn-, and post-collisional evolution. *Journal of the Virtual Explorer*, *08*, 55–74. https://doi.org/10.3809/jvirtex.2002.00058

Vergés, J., Millán, H., Roca, E., Muñoz, J. A., Marzo, M., Cirés, J., et al. (1995). Eastern Pyrenees and related foreland basins: Pre-, syn- and post-collisional crustal-scale cross-sections. *Marine and Petroleum Geology*, *12*(8), 903–915. https://doi.org/10.1016/0264-8172(95)98854-X

Vermeesch, P., & Tian, Y. (2014). Thermal history modeling: HeFTy vs. QTQt. *Earth-Science Reviews*, *139*, 279–290. https://doi.org/10.1016/j.earscirev.2014.09.010

Vignaroli, G., Faccenna, C., Jolivet, L., Piromallo, C., & Rossetti, F. (2008). Subduction polarity reversal at the junction between the Western Alps and the northern Apennines, Italy. *Tectonophysics*, *450*(1–4), 34–50. https://doi.org/10.1016/j.tecto.2007.12.012

Viola, G., Odonne, F., & Mancktelow, N. S. (2004). Analogue modeling of reverse fault reactivation in strike-slip and transpressive regimes: Application to the giudicarie fault system, Italian Eastern Alps. *Journal of Structural Geology*, *26*(3), 401–418. https://doi.org/10.1016/j.jsg.2003.08.014

Wagner, G. A., Reimer, G. M., & Jäger, E. (1977). Cooling ages derived by apatite fission track, mica Rb-Sr and K-Ar dating: The uplift and cooling history of the central Alps. *Memorie di Scienze Geologiche*, *30*, 1–27.

Waldner, M., Bellahsen, N., Mouthereau, F., Bernet, M., Pik, R., Rosenberg, C. L., & Balvay, M. (2021). Central Pyrenees Mountain building: Constraints from new LT thermochronological data from the Axial Zone. *Tectonics*, *40*(3). https://doi.org/10.1029/2020TC006614

Wessel, P., Luis, J. F., Uieda, L., Scharroo, R., Wobbe, F., Smith, W. H. F., & Tian, D. (2019). The generic mapping tools version 6. *Geochemistry, Geophysics, Geosystems*, *20*(11), 5556–5564. https://doi.org/10.1029/2019GC008515

Whitchurch, A. L., Carter, A., Sinclair, H. D., Duller, R. A., Whittaker, A. C., & Allen, P. A. (2011). Sediment routing system evolution within a diachronously uplifting orogen: Insights from detrital zircon thermochronological analyses from the south-central Pyrenees. *American Journal of Science*, *311*(5), 442–482. https://doi.org/10.2475/05.2011.03

Wu, L., Monié, P., Wang, F., Lin, W., Ji, W., Bonno, M., et al. (2016). Cenozoic exhumation history of Sulu terrane: Implications from (U-Th)/He thermochrology. *Tectonophysics*, *672–673*, 1–15. https://doi.org/10.1016/j.tecto.2016.01.035

Ziegler, P. A. (1992). European Cenozoic rift system. *Tectonophysics*, *208*(1–3), 91–111. https://doi.org/10.1016/0040-1951(92)90338-7

Reference From the Supporting Information

Sun, S. S., & McDonough, W. F. (1989). Chemical and isotopic systematics of oceanic basalts: Iimplications for mantle composition and processes. *Geological Society, London, Special Publications*, *42*, 313–345. https://doi.org/10.1144/GSL.SP.1989.042.01.19